RESEARCH ARTICLE

Decompression and degassing, repressurization, and regassing during cyclic eruptions at Guagua Pichincha volcano, Ecuador, 1999–2001

H. M. N. Wright[1] · R. Cioni[2] · K. V. Cashman[3] · P. Mothes[4] · M. Rosi[2]

Abstract

In 1999–2001, Guagua Pichincha volcano, Ecuador, produced a series of cyclic explosive and effusive eruptions. Rock samples, including dense blocks and pumiceous clasts collected during the eruption sequence, and ballistic bombs later collected from the crater floor, provide information about magma storage, ascent, decompression, degassing, repressurization, and regassing prior to eruption. Pairs of Fe-Ti oxides indicate equilibrium within 1.2–1.5 log units above the NNO oxidation buffer and equilibrium temperatures from 805 to 905 °C. Melt inclusions record H_2O contents of 2.7–4.6 wt% and CO_2 contents (uncorrected for CO_2 segregation into bubbles) from 19 to 310 ppm. Minimum melt inclusion saturation pressures fall between 69 and 168 MPa, or equilibration depths of 2.8 and 6.8 km, the lower end of which is coincident with the maximum inferred equilibration depths for the most vesicular breadcrust bombs sampled. Amphibole phenocrysts lack breakdown rims (except for one sample) and plagioclase phenocrysts have abundant oscillatory compositional zones. Plagioclase areal microlite number densities (N_a) range over less than one order of magnitude (8.9×10^3–8.7×10^4 mm^{-2}) among all samples, with the exception of a dense, low crystallinity sample ($N_a = 3.0 \times 10^3$ mm^{-2}) and a pumiceous sample erupted on 17 December 1999 ($N_a = 1.7 \times 10^3$ mm^{-2}). Plagioclase microlite shapes include tabular, hopper, and swallowtail forms. Taken together, the relatively high plagioclase microlite number densities, the high number of oscillatory zones in plagioclase phenocrysts, the presence of CO_2 in groundmass glass, seismicity, and time-varying tilt cycles provide a picture of sudden evacuation of magma residing at different levels in the shallow conduit. Explosive eruptions punctuate inter-eruptive repose periods marked by time-varying rates of degassing (volatile fluxing) and re-pressurization. Shallow residence time in the conduit was sufficient to allow precipitation of silica-phase in the groundmass, but insufficient to allow breakdown of hornblende phenocrysts, with the one exception of the final dome sample from 2000, which has the longest preceding repose time. These results support a model of cyclic pressure cycling, volatile exsolution and regassing, and magma decompression decoupled from ascent.

Keywords Microlites · Crystal size distribution · Guagua Pichincha · Eruption style · Magma decompression · Degassing · Outgassing

✉ H. M. N. Wright
hwright@usgs.gov

1 U.S. Geological Survey, Volcano Disaster Assistance Program 1300 SE Cardinal Court, Vancouver, WA 98683, USA

2 Dipartimento Scienze della Terra, Univ. Pisa, Via S. Maria, 53, 56126 Pisa, Italy

3 Department of Earth Sciences, University of Oregon, Eugene, OR 97403, USA

4 Instituto Geofísico, Escuela Politecnica Nacional Casilla 1701-2759, Quito, Ecuador

Introduction

At a single volcano, and even for a single magma composition, volcanic eruption style can vary widely because it depends, in large part, on the dynamics and extent to which magma can degas and outgas (and sometimes regas, wherein gas from depth equilibrates with host melt) en route to the surface. Several authors have recognized the importance of decompression rate and outgassing efficiency on eruptive behavior, where the slowest decompression and greatest ease of gas escape allow effusive extrusion of lava, and rapid decompression and restricted gas loss cause the most explosive magmatic eruption styles (Cashman 2004; Gonnermann and Manga 2013; Cassidy et al. 2018). Variations in decompression rate can cause eruptive style to change in a single eruption sequence and are recorded in the eruptive products of that sequence. Dome-forming eruptions, in particular, provide a clear example of time variation in eruptive style and resulting hazards. At Guagua Pichincha, low-hazard lava effusion is commonly punctuated by explosive eruptions (cf. Ogburn et al. 2015), most of which are small in volume and low in intensity (Volcanic explosivity index, VEI ≤3; magnitude, M<4; intensity, I<7). These sequences can, however, include larger explosive events, which present challenges for successful eruption forecasting and risk mitigation. Crystals and bubbles preserved within eruptive products from these sequences provide records of the decompression and ascent histories that preceded eruption, thereby supplying information about the subsurface controls on eruptive style (e.g., Cashman and McConnell 2005; Clarke et al. 2007; Martel 2012).

Decompression and/or H_2O exsolution can trigger magma crystallization within the shallow crust. Rapid magma decompression causes relatively high degrees of undercooling where crystal nucleation dominates over growth, producing abundant microlites (e.g., Geschwind and Rutherford 1995; Hammer and Rutherford 2002; Couch et al. 2003), whereas slow magma decompression often causes growth on pre-existing crystals (e.g., Brugger and Hammer 2010; Martel 2012; Riker et al. 2015; Befus and Andrews 2018), perhaps to the exclusion of microlite formation (Cashman 2020). Given the variation in rates of crystal nucleation and growth with degree and duration of undercooling, products from eruption sequences at intermediate-composition stratovolcanoes around the world have been used to infer pre-eruptive conduit stratigraphy (vertical variation in magma properties). Correlations have been documented between microlite crystallinity and pre-explosive-eruption repose time (Hammer et al. 1999), eruption style (Taddeucci et al. 2004; Wright et al. 2012; Cioni et al. 2014), and pre-eruptive conduit stratigraphy (Cashman and McConnell 2005; Clarke et al. 2007); microlite crystallinity has also been

inversely correlated with effusion rate (Nakada and Motomura 1999). Similarly, microlite number density has been correlated with eruption style (Benage et al. 2021) and with dome effusion rate (Hammer et al. 2000). Furthermore, textural evidence from many studies suggests that formation of strongly degassed and densified (outgassed) plug/dome material may help pressurize the system prior to Vulcanian explosive eruptions (Wright et al. 2007; Soufriere Hills, Burgisser et al. 2010; Merapi, Preece et al. 2016; Galeras, Bain et al. 2019; Tungurahua volcano, Gaunt et al. 2020). Here, we use the products of explosive eruptions within a dome-forming eruption sequence at Guagua Pichincha volcano in 1999–2001 to better understand the conditions that produced the repeated cycle of Subplinian to Vulcanian eruptions followed by dome effusion that characterized this eruptive episode. Conversely, we assess the textural and compositional attributes of resulting pyroclasts that may uniquely indicate cyclic activity.

Background and the 1999–2001 eruptions of Guagua Pichincha volcano

Guagua Pichincha dacitic stratovolcano is the active volcanic center of the Pichincha Volcanic Complex, located 12 km west of Quito, Ecuador (Fig. 1), in the Northern Volcanic Zone of the South American Andes. Volcanic activity began at Guagua Pichincha 55,000 years ago with effusive andesitic to dacitic eruptions (Barberi et al. 1992;

Fig. 1 Map of active volcanoes in Ecuador showing location of Guagua Pichincha volcano

Fornari et al. 2004). Cone construction and evolution continued through a series of andesitic–dacitic explosive and effusive eruptions, phreatic explosions, and sector collapse events (Barberi et al. 1992; Hall 1977; Monzier et al. 2002). Late Holocene activity has included at least three, and perhaps four, 100–200-year eruptive cycles within the past 2000 years, where eruptions progressed from dominant dome-formation and Vulcanian–Subplinian ashfall and pyroclastic flow generation to a culminating Plinian eruption at the end of the cycle (Barberi et al. 1992; Hall 1977; Robin et al. 2008). The most recent major eruption occurred in 1660, preceded by minor eruptions in 1566, 1575, and 1582 CE. Phreatic activity has also occurred throughout historical times.

The most recent eruptive period began with low-level phreatic activity in 1830–1831, 1868–1869, 1881, and then again in 1980–1981, 1988, and 1993 (Robin et al. 2008), likely resulting from pressurization of SO_2-rich magmatic fluids (Chiodini et al. 1992), although later phreatic events have also been correlated with rainy periods (for example, in 2002). In May 1997, a swarm of distal VT-type (volcano-tectonic) seismic events occurred approximately 15 km northeast of the volcano (Villagómez 2000; Legrand et al. 2002), increasing in number in June 1998 toward a peak in August 1998. Phreatic activity also intensified in August and the number of long-duration tremor, VT, and shallow LP (long period) and hybrid earthquakes increased (Villagómez 2000; Garcia-Aristizabal et al. 2007). In June 1999, a swarm of VT earthquakes accompanied ash-rich phreatic explosions. A final VT swarm from 8 to 24 September and a subsequent LP swarm on 25 September preceded the first magmatic eruption on 26 September 1999.

The ensuing eruptive sequence consisted of several Vulcanian and Subplinian eruptions, construction, and destruction of seven domes between late September and mid-December 1999, construction of an eighth dome in late December that was destroyed in July 2000 (Global Volcanism Program 2001), and construction of a ninth dome in mid to late-2000 that persists today (Table 1;

Mothes et al. 2002). The first dome emerged on 28 September 1999, when tiltmeters on the caldera rim showed an inflationary response of 12 microradians that correlated with vigorous dome growth (Mothes et al. 2000). The dome persisted until 5 October, when it was destroyed by a Subplinian eruption, the largest of the eruptive sequence that produced 2mm of ash fall in Quito and caused the Quito International Airport to close. The 5 October eruption cloud reached 15 km above the summit (Washington VAAC 1999OCT05/2225Z). A second Subplinian eruption on 7 October produced a 13- to 15-km high eruption cloud (Washington VAAC 1999OCT07/1330Z) and generated a pyroclastic flow that traveled down the Rio Cristal to the west. After 7 October, dome growth occurred without accompanying explosions until this relative quiescence ended on 10 November with another Vulcanian eruption. Dome regrowth and Vulcanian dome-destroying eruptions then occurred at approximately one-week intervals through November and December; frequent LP seismicity and infrequent VT seismicity accompanied explosions and eruptions throughout this period (Fig. 2). As in Wright et al. (2007), we use the term explosion to refer to explosion seismic signals, eruption to denote ejection of material from the vent, and fragmentation to represent the transition from a continuous melt or solid phase containing bubbles to a continuous gas phase containing parcels of bubbly melt/solid. During this period, eruption columns reached $\leq$ 10 km above the summit and several dusted Quito with ash. Each Vulcanian eruption was short, accompanied by several seismic explosion signals and involved a small volume of magma (Global Volcanism Program 1999). Importantly, domes continued to extrude from the same location, indicating that the vent location did not migrate. Repeat observations of dome dimensions through time show that dome growth rates reached 1.7 m^3/s but averaged 0.5 m^3/s (Table 1, Mothes et al. 2002). Some dome collapses were associated with volcanic explosions, but most collapses were the result of oversteepening of the dome and occasionally generated pyroclastic

Table 1 Dome volumes based on visual observations of dome dimensions (Mothes et al. 2002)

Dome growth dates	Dome	Dome volume (m^3)	Growth rate (m^3/s)	Dome dimensions (m)
28-Sep to 7-Oct 1999	#1	900,000	0.7	$110 \times 170 \times 50$
08-Oct to 10-Nov 1999	#2	780,000	0.27	$100 \times 150 \times 50$
11- to 17-Nov 1999	#3	400,000	0.66	$200 \times 150 \times 30$
18- to 26-Nov 1999	#4	380,000	0.49	$200 \times 130 \times 30$
27-Nov to 03-Dec 1999	#5	380,000	0.55	$200 \times 130 \times 30$
04- to 10-Dec 1999	#6	500,000	0.83	$100 \times 150 \times 30$
11- to 17-Dec 1999	#7	1,200,000	1.7	$200 \times 150 \times 70$
18-Dec 1999 to 24-Jul 2000	#8	3,800,000	0.2	$310 \times 220 \times 70$
25-Jul 2000 to 26-Mar 2001	#9	5,400,000	0.1	$340 \times 220 \times 90$

Fig. 2 Timeline of pre-eruptive and syn-eruptive monitoring data and eruptive activity from December 1997 to December 2000. Seismic data only shown through April 2000, from Villagómez (2000). LPs are long period earthquakes, VTs are volcano tectonic earthquakes, MPs are medium period earthquakes, and dVTs are distal VT earthquakes
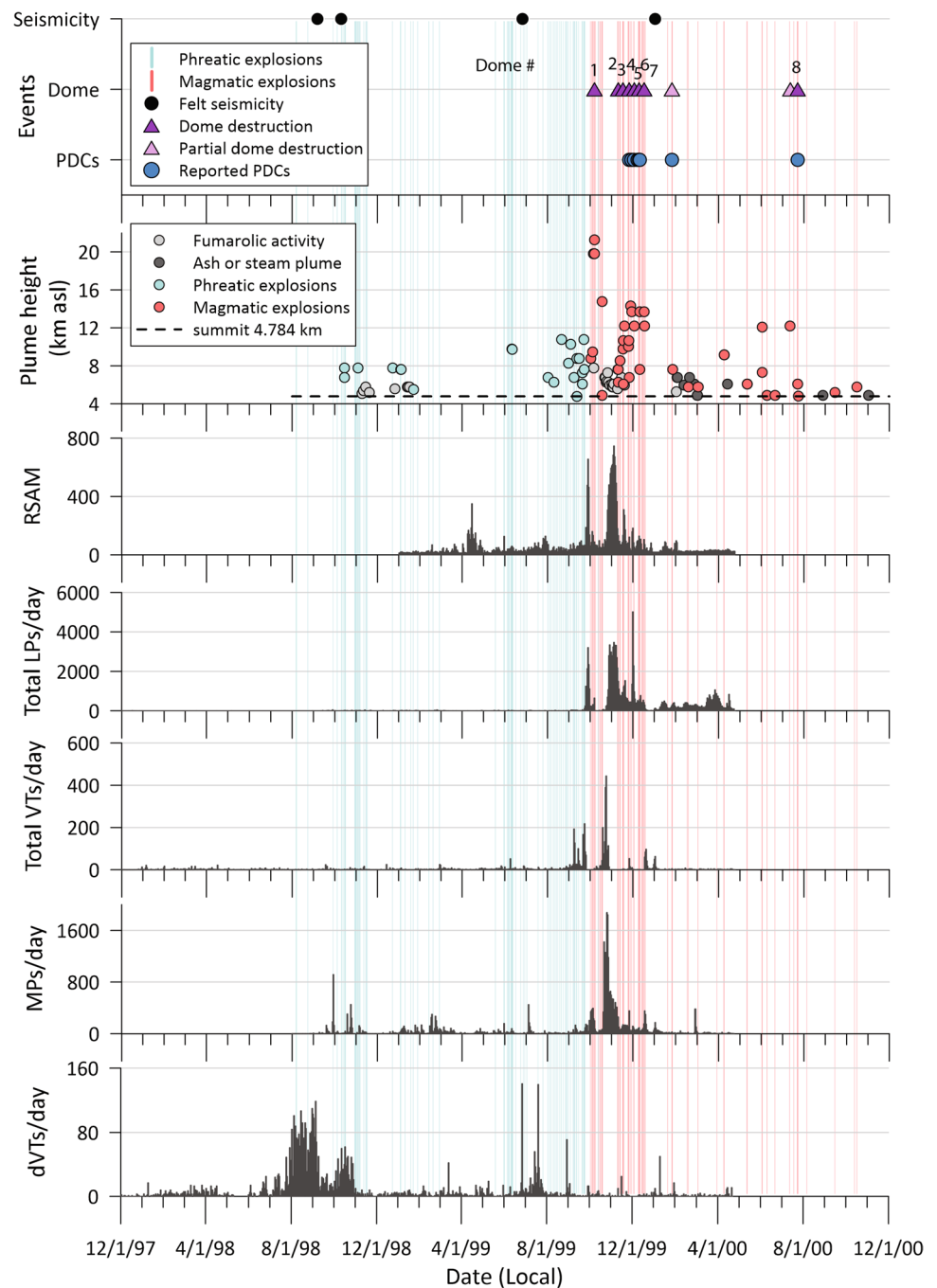
flows. In general, increases in long-period seismic activity both preceded and accompanied dome emplacement, after which seismic activity diminished while the dome continued to grow to its maximum size, until one or more explosions destroyed it.

Early phreatic eruptions produced dense ash and pyroclasts of old, recycled edifice material. Juvenile pumice of dacitic composition began to appear in ash emissions starting on 26 September. The 5 and 7 October Subplinian eruptions produced larger volumes of similar juvenile

pumice (Global Volcanism Program 1999). Pyroclastic density currents (PDCs) generated in several of the dome collapse and Vulcanian eruptions traveled west down the Rio Cristal. PDCs produced on 7 October were modest in runout distance, but subsequent Vulcanian dome-collapse events (i.e., 26 November 1999) produced PDCs with runout to 11 km.

Deposits from Vulcanian eruptions at Guagua Pichincha include a thin fine-ash bed, channelized deposits of block and ash flow-type PDCs that include breadcrusted blocks,

and abundant ballistic bombs that cover the surface of Guagua Pichincha's summit crater. Wright et al. (2007) documented four textural categories of ballistic bombs found on the crater floor, including dense bombs (DB), thickly breadcrusted bombs (TkB), thinly breadcrusted bombs (TnB), and foliated intermediate bombs (FIB). Groundmass H_2O and CO_2 contents (max 3.1 wt% H_2O, max 17 ppm CO_2; not from the same bomb) preserved in quenched bomb rinds were used to infer pre-eruptive staging depths reaching 2.8 km, but dominantly <1.5 km beneath the summit (max 69 MPa, all except one sample <36 MPa; Wright et al. 2007). The presence of ppm levels of CO_2 in groundmass glass provides evidence of pre-eruptive regassing/equilibration with gas from unerupted magma at depth. Together, these observations suggest eruptive cycles that included: (1) explosive eruption, (2) depressurization of underlying magma that caused magma degassing and permeable gas escape, (3) slow magma ascent and conduit refilling accompanied by microlite crystallization and conduit densification/regassing (here, regassing is used to describe an increase in dissolved volatile content as melt equilibrates with gas from depth), and (4) dome extrusion and formation of a dense conduit plug. Here, we build upon this work to document textural and compositional characteristics of the same ballistic bombs, likely erupted from Vulcanian eruptions, as well as dense and pumiceous clasts from the 26 September phreatomagmatic eruption, 5 and 7 October Subplinian eruptions, and 29 November, 17 December 1999, 17 July, and 30 August 2000 small Vulcanian and dome-building eruptions. We examine crystal textures and clast compositions, focusing on characterization of plagioclase microlites and groundmass glass compositions, to better understand the roles of decompression, degassing, and ascent on eruption style in 1999–2000 eruptions of Guagua Pichincha.

Methods

Melt inclusions

Concentrations of H_2O and CO_2 were measured by Fourier transform infrared spectroscopy (FTIR) in melt inclusions hosted in plagioclase and pyroxene from pumice erupted on 5 and 7 October and from two breadcrust bombs erupted in subsequent undated Vulcanian eruptions. After selection of melt inclusions based on their integrity and glassy character, host crystals were glued to a glass slide with crystal bond, polished on both sides, then removed from the glass slide and rinsed in acetone and ethanol. Thickness was measured with an electronic micrometer (Mitutoyo Digimatic Indicator) with a precision of 1 μm. For wafers too thin to be safely measured with the micrometer, thickness was measured on

a scaled image of crystal depth, taken after having fixed the crystal on an adhesive strip and placed it vertically under an optical microscope. For each crystal, three measurements were made as close as possible to the melt inclusion, and their arithmetic mean calculated.

We used a Nicolet Magna 560 spectrometer equipped with a NicPlan infrared microscope (Earth Sciences Department of the University of Pisa). The methods of melt inclusion preparation for FTIR analysis and recalculation are described in Cioni (2000). Wafer thickness, melt inclusion dimensions, and peak absorbances are recorded in Supplementary Data (Tables 1-3SM). Bubble diameters were also tabulated for the most representative melt inclusions; maximum calculated ratios between bubble and melt inclusion volumes range from 1 to 7%. We assume a glass density of 2350 g cm^{-3}. Spectra were taken with a resolution of 4 cm^{-1} and between 512 and 1024 scans. Absorbances were measured from peak heights after subtraction of the background signal, extrapolated with a flexible drawing curve.

The concentration of the absorbing species was calculated using the Beer-Lambert law:

$$c_i = 100 \times \left(MW_i A\right) / \left(d\rho\varepsilon_i\right)$$

where c_i = species concentration, in wt%; MW_i = molecular weight of the ith species in g mol^{-1}; A = absorbance in cm^{-1}; d = sample thickness, in cm; ρ = sample density in g/cm^3; ε_i = molar absorptivity of the ith species, in L mol^{-1} cm^{-1}.

Molecular H_2O and OH$^-$ species were measured using the absorbance value at 5200 and 4500 cm^{-1}; total water was calculated as the sum of the concentrations resulting from the two peaks. Values of 1.61 and 1.73 L/(mol cm) were used for the molar absorptivity coefficients of the two species, respectively (Newman et al. 1986). Concentration of molecular CO_2 was calculated using the 2350 cm^{-1} peak and a molar absorptivity coefficient of 1214 L/(mol cm) (Behrens et al. 2004). CO_2 concentrations measured in this way are minimum estimates because they do not account for CO_2 segregation into vapor bubbles (Moore et al. 2015). Two to four spectra were collected on each melt inclusion, and the arithmetic mean of the resulting concentration calculated.

Electron microprobe

Thin sections of both the vesicular core and dense rind of each breadcrust bomb sample were prepared for analysis on a Cameca SX50 electron microprobe at the University of Oregon and a JEOL 8900 electron microprobe at the USGS, Menlo Park, California, for major oxide analyses. A 15-kV electron beam at 20 nA with a 5-μm diameter defocused spot was used to analyze groundmass glass compositions and melt inclusions in plagioclase and pyroxene phenocrysts. Volatile

migration due to sample bombardment (and heating) by the electron beam was corrected using an extrapolation method in the software package Probe for Windows® (Donovan 2002). Water contents in melt inclusion glass were estimated using the water-by-difference method in Probe for Windows® software. This method iteratively recalculates melt compositions by adjusting water content until totals reach 100%, thereby compensating for the effect of water on the routine matrix correction (Roman et al. 2006). Although the WBD method is not as precise as FTIR spectroscopic techniques, our results show good agreement between the two techniques. Plagioclase microlite compositions were analyzed with a 10-kV focused electron beam at 20 nA. Fe-Ti oxide compositions were analyzed with a 15-kV focused electron beam at 30 nA.

SEM-EDS

Major element concentrations of minerals and melt inclusions were also analyzed with an energy dispersive X-ray microanalysis using EDAX DX4 on a Philips XL30 SEM at the Dipartimento di Scienze della Terra of Pisa, at an accelerating voltage of 20 kV, beam current of 0.1 nA and working distance of 10 mm. A comparison between EDS compositional analyses and standard compositions are listed for three volcanic glass standards in Supplementary Material (Table 4SM). Melt inclusion composition is reported as the average of 2 to 4 analyses.

Textural analysis

Textural characteristics of both crystals and vesicles were analyzed using an optical microscope and SEM images. Phenocryst abundance was determined by 500 point counts on one thin section of each sample. Error due to sample heterogeneity is approximately 7% of modal percentage measured (determined from replicate point counts of the same sample). Vesicle abundance was determined only in the breadcrust bomb rinds, which were not sufficiently large for bulk analysis used to measure overall bomb density (Wright et al. 2007). Here, BSE images at 100× magnification provided sufficient coverage for areal analysis of vesicle content and for imaging and analysis of ubiquitous zoned plagioclase crystals, where analysis involved counting the numbers of oscillatory zones. Many of these oscillatory-zoned plagioclase crystals contain high-An zones that truncate interior zonation patterns (black arrows point to truncation surfaces in Fig. 5). Where truncation surfaces are present, only those oscillatory zones rimward of the high-An truncation zone were counted. High magnification (1000×) BSE images were used for quantitative analysis of groundmass crystalline phases and inspection of hornblende rim textures.

BSE images were obtained on a JEOL 6300 scanning electron microscope at the University of Oregon using a 10-kV electron beam at 10–20 nA sample current and a 15-mm working distance. Between 300 and 1200 crystals of each sample were hand-digitized to obtain representative measurements (analysis of 2–4 images per sample). Two samples showed pronounced alignment of microlites and vesicles (at both macroscopic and microscopic scales); to fully characterize the bubble and crystal textures in these clasts, images were obtained for two perpendicular sections. Image analysis was performed using the public domain NIH ImageJ program (Schneider et al. 2012).

Plagioclase is the most abundant and largest microlite species, although mafic phases are also variably present. Areal number densities (number of crystals/mm^2, N_a) of both plagioclase and mafic microlites were determined by counting crystals fully enclosed in each image plus those crystals cut by the lefthand and upper margins and dividing the total number by the image area corrected for the vesicle area. Microlites were distinguished from microphenocrysts by size (microlites < 30-μm maximum dimension) and from crystal fragments by the absence of chemical zonation.

Crystal size distributions (CSDs; Marsh 1988, determined using CSDCorrections of Higgins 2000) were determined for plagioclase microlites to compare the kinetics of crystallization among samples. To convert two-dimensional textural data to three-dimensional population information, we used the program CSDslice (Morgan and Jerram 2006) to approximate the three principal crystal axis dimensions (short, S; intermediate, I, and long, L). Mangler et al. (2022) demonstrated that crystal shape varies with crystal size in many dome-forming volcanic sequences, and therefore the assumption of constant crystal shape may be inaccurate. For prismatic crystals, the minor axes of 2D best-fit ellipses represent the most likely intersection planes between crystals and the plane of the thin section. Shape-corrected volumetric number densities are calculated based on linear fits to shape-corrected CSD data. For the majority of samples, two linear CSD segments were fit to the data. We plot volumetric number densities based on the smallest crystals (steepest best-fit lines in Fig. 9), shown as N_T in this manuscript, but data for all segments are included in the Supplementary Files (Table 5SM). To compare with previous published microlite studies, we present both uncorrected 2D and corrected 3D information here.

Variation in crystal habit of plagioclase microlites was quantified using two additional measures of shape. The aspect ratio is the ratio of the short to the long axes S/L fit to 2D data using CSDSlice (as calculated above; Higgins 1994) and the formfactor (F) is calculated as $F = 4\pi A / P^2$, where A and P are the area and the perimeter, respectively, of the crystal. Aspect ratio provides a quantitative description of 3D crystal elongation. Perfectly equant crystals have aspect ratios of 1.0; lower aspect ratios represent more elongate crystals. For a perfect circle $F = 1$; as the crystal perimeter becomes more convolute, F goes to 0. Measurements are
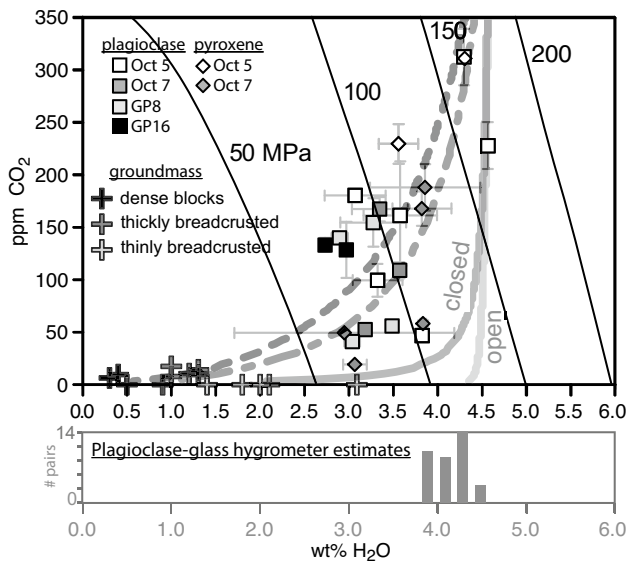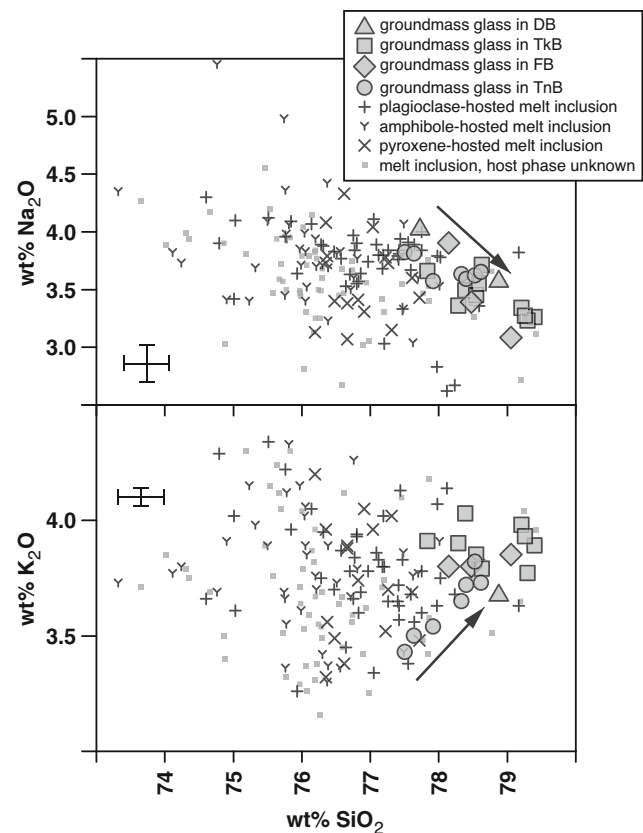
Fig. 3 Melt inclusion H_2O versus CO_2 concentrations from Guagua Pichincha pumice clasts produced during Subplinian eruptions on 5 and 7 October 1999 and from bombs erupted in later Vulcanian eruptions (GP8 and GP16). Isobars calculated using VolatileCalc (Newman and Lowenstern 2002). Histogram at bottom shows calculated equilibrium H_2O concentrations for touching plagioclase microlite/ phenocryst rim and surrounding groundmass glass compositions (Waters and Lange 2015). Groundmass glass H_2O versus CO_2 concentrations of dense and breadcrust bombs shown for comparison from Wright et al. (2007). Degassing paths were calculated using Newman and Lowenstern (2002): light gray solid line is the open system degassing model, dark gray solid line is closed system degassing, dash-dotted line is closed system degassing in the presence of 1 wt% vapor, and short-dashed line is closed system degassing with 2 wt% vapor
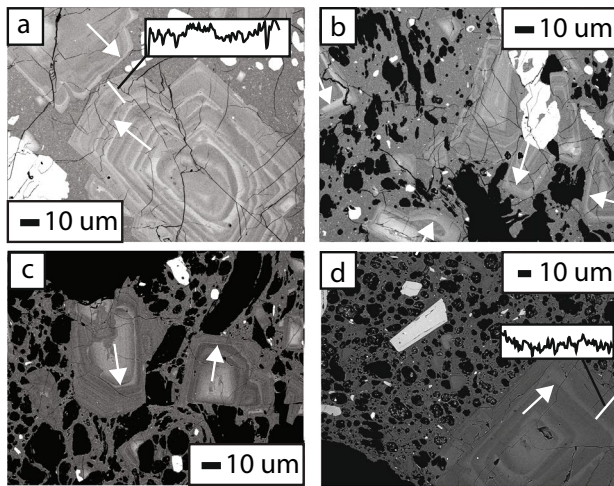

Fig. 4 Glass compositions of melt inclusions and groundmass glass of analyzed breadcrust bombs and dense bombs. Arrows point in the direction of progressive crystallization in the absence of a silica phase

Results

FTIR melt inclusion analyses

Glassy melt inclusions are especially abundant in orthopyroxene, clinopyroxene, and plagioclase, where they are commonly found along numerous, compositionally distinct growth zones. Melt inclusion H_2O and CO_2 concentrations overlap between samples although melt inclusions from the 5 October pumice reach the highest volatile concentrations ($H_2O = 3.1–4.6$ wt%; $CO_2 = 46–310$ ppm; Table 1SM; Fig. 1SM; Fig. 3). Melt inclusions from the 7 October pumice and from breadcrust bomb samples GP8 and GP16 have $H_2O = 2.7–3.9$ wt% and $CO_2 = 19–190$ ppm. Pyroxene and plagioclase-hosted melt inclusions contain similar volatile concentrations. As noted above, reported CO_2 concentrations are minima because of the possible segregation of CO_2 in shrinkage bubbles (Moore et al. 2015).

Glass compositions

Groundmass glass compositions are uniformly rhyolitic (77.5 to 79.4 wt% SiO_2; Table 6SM), with significant overlap between bomb morphology groups. K_2O generally increases and CaO and Na_2O decrease with increasing SiO_2 content (Fig. 4). Melt inclusion glass compositions cover a broader range, from 73.6 to 79.3 wt% SiO_2, with 0–5.2 wt% volatiles by difference. Some of this variation may be due to post-entrapment modification of glasses via crystallization of the host mineral along melt inclusion-host interface. Groundmass glass compositions bound melt inclusion contents along a trend consistent with crystallization in the absence of a silica phase.

Crystal compositions

Touching titanomagnetite and ilmenite pairs are sparse within Guagua Pichincha ballistic bombs. Representative compositions of touching pairs in these bombs are shown in Supplementary Data (Table 7SM). All pairs lack evidence for compositional zonation and are in contact with groundmass glass.
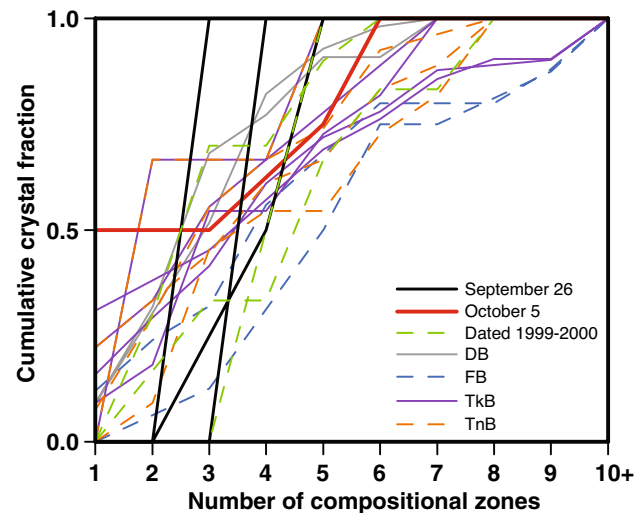
made using images at similar scales to avoid problems with resolution-dependent shape analysis (cf. Liu et al. 2015).

Fig. 5 (**a-d**) Backscatter electron images of oscillatory zoned plagioclase phenocrysts that are abundant in all samples, including GP8 (**a**), GP17b (**b**), GP3 (**c**), and 26 September 1999 (**d**). White arrows point to BSE bright zones (An-rich) that truncate zonation patterns in crystal interiors. Line profiles in panels a and b show the variation in backscatter electron image grayscale values across the white line profile shown for example

Fig. 6 Cumulative frequency plot of the number of oscillatory zones exterior to the outermost compositional truncation surface in plagioclase crystals. Note that the lowest number of compositional zones are found in samples from the first magmatic eruption on 26 September 1999

Plagioclase phenocryst compositions are An_{32-69} in pumice from 5 October, An_{38-67} in pumice from 7 October, and An_{27-69} in ballistic blocks. Microlite compositions are An_{35-53} in ballistic blocks (Table 4). Compositional zonation in phenocrysts is commonly oscillatory in character (Fig. 5), with significant overlap between core and rim compositions (Table 8SM).

Crystal textures

Phenocryst textures are similar in all samples. The dominant phenocryst phase is plagioclase, followed by amphibole (magnesium hornblende with some tschermakite and magnesium hastingsite; Garcia-Aristizabal et al. 2007), Fe-Ti oxides, and orthopyroxene, with minor amounts of apatite and clinopyroxene (Table 3). Individual clasts vary in phenocryst content, however. Total phenocryst crystallinity in ballistic bomb samples ranges from 31% in thinly breadcrusted sample GP5 to 51% in thickly breadcrusted sample GP9. This difference primarily reflects differences in plagioclase crystallinity (23 and 39%, respectively). On average, ballistic bomb samples have 41% (st. dev. = 5%) phenocrysts, of which 31% (st. dev. = 4%) are plagioclase. Plagioclase phenocrysts are typically oscillatory zoned with normally zoned rims. Of these zoned crystals, most contain at least one, and in some cases several, particularly An-rich zones that truncate interior zonation patterns (Fig. 5; Table 8SM; Fig. 2SM). The number of oscillatory zones exterior to the outermost truncation surfaces ranges from 1 to 15, with most showing between 1 and 7 oscillations

(Fig. 6). Samples erupted in the first magmatic eruption on 26 September 1999 contain crystals with the lowest maximum number of oscillatory zones. Samples from 5 October 1999 contain fewer oscillatory zones than those from most dated and undated Vulcanian eruptions, as well as of the ballistic material. The highest numbers of oscillatory zones are found in thickly breadcrusted (TkB) and foliated intermediate bombs (FIB). Less abundant amphibole phenocrysts
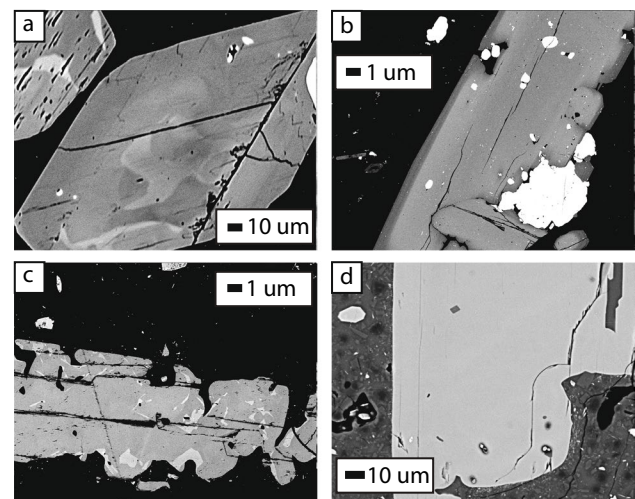
Fig. 7 Amphibole textures in analyzed samples range from intact to small amounts of resorption in GP-17a (**a**) to clear resorption and Mg-rich rim growth in GP-8 (**b**), or extensive resorption in GP-6 (**c**). Only the dome sample from 30 August 2000 (**d**) contains amphibole with poorly developed breakdown rims in the lower right side of the panel (300800)
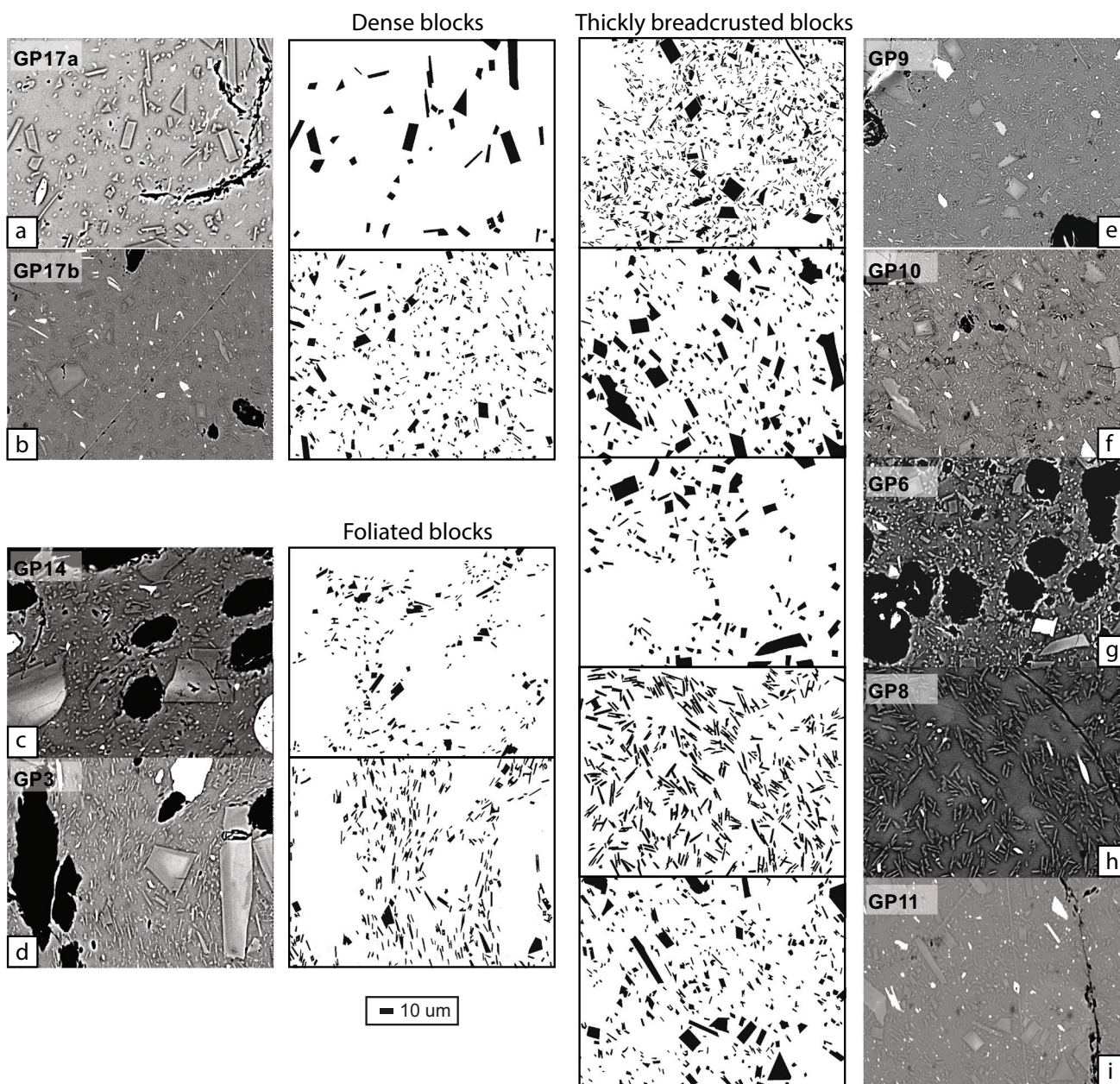
Fig. 8 SEM backscatter electron images of undated dense (**a-b**) and breadcrust bombs (**c-n**), in addition to dated samples (**o-z**) are shown, grouped by surface texture and/or date of eruption. Mafic microlites (pyroxenes and oxides) are white, plagioclase microlites are light gray, groundmass glass is medium to dark gray, silica-phase crystals are darkest gray, and vesicles are black in BSE images. Paired binary images are shown next to the corresponding BSE image, showing plagioclase microlites that were used for textural characterization

lack breakdown rims, except in the dense sample from the final dome (30 August 2000) where breakdown rims measure 2-–4-μm width. Some hornblende phenocrysts also have resorbed margins (Fig. 7).

Microlite phases include dominant plagioclase crystals, lesser amounts of mafic crystals (<2% of groundmass) and limited silica-phase crystals in the groundmass of several ballistic bomb samples, early phreatomagmatic samples from 26 September 1999, and dense samples erupted in 2000 (Fig. 8;

Table 2; Fig. 3SM). Plagioclase microlite number densities span less than one order of magnitude (8.9×10^3–8.7×10^4 mm^{-2}) among all samples, with the exception of two samples with lower number densities: GP-17a (DB), a dense, low crystallinity sample ($N_a = 3.0 \times 10^3$ mm^{-2}) and 991217, a pumiceous sample erupted on 17 December 1999 ($N_a = 1.7 \times 10^3$ mm^{-2}; Table 2). These areal number densities correspond to volumetric number densities calculated from fits to the smallest crystals in CSD plots (steep CSD slopes, Fig. 3SM,
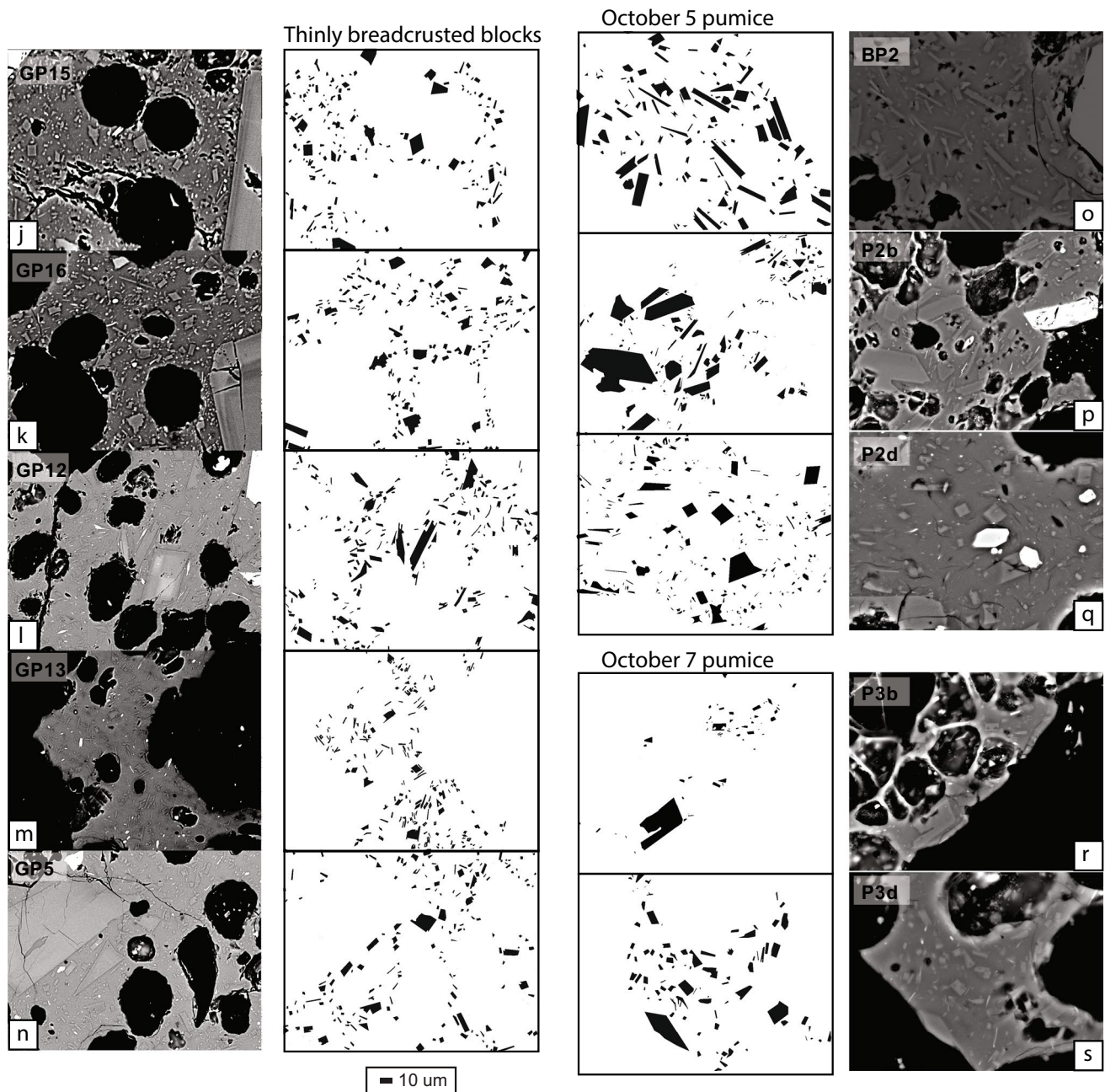
Fig. 8 (continued)

Table 5SM; Table 2) $N_T = 3.4 \times 10^6$–3.7×10^7 mm$^-$, with the low crystallinity outlier GP-17a, $N_T = 2.6 \times 10^5$ mm^{-3}.

CSDs typically form two linear segments, with a decrease in slope at larger microlite sizes that suggest a multi-stage crystallization history (Table 5SM). Multi-stage crystallization history is consistent with oscillatory zonation of phenocryst margins. In most samples, characteristic plagioclase microlite sizes as calculated from negative 1/CSD slope (L_d) vary by a factor of less than 4 (2 to 7 μm) and N_T varies by only an order of magnitude. DB sample GP17a is again an

exception, with low plagioclase groundmass crystallinity (φ = 9%) and plagioclase microlite N_T (1.1×10^5 mm^{-3}) and high L_d (13 μm). Plagioclase crystallinity in general (x_{pl}) is higher in thickly breadcrusted bombs (average x_{pl} = 17%) than in thinly breadcrusted bombs (average x_{pl} = 12%), although there appears to be as much variation in crystal texture within bomb type as among bomb classes. This is illustrated by the range in crystal size and number density seen in thickly breadcrusted samples GP8 and GP9 (Fig. 8c, d; Table 2).
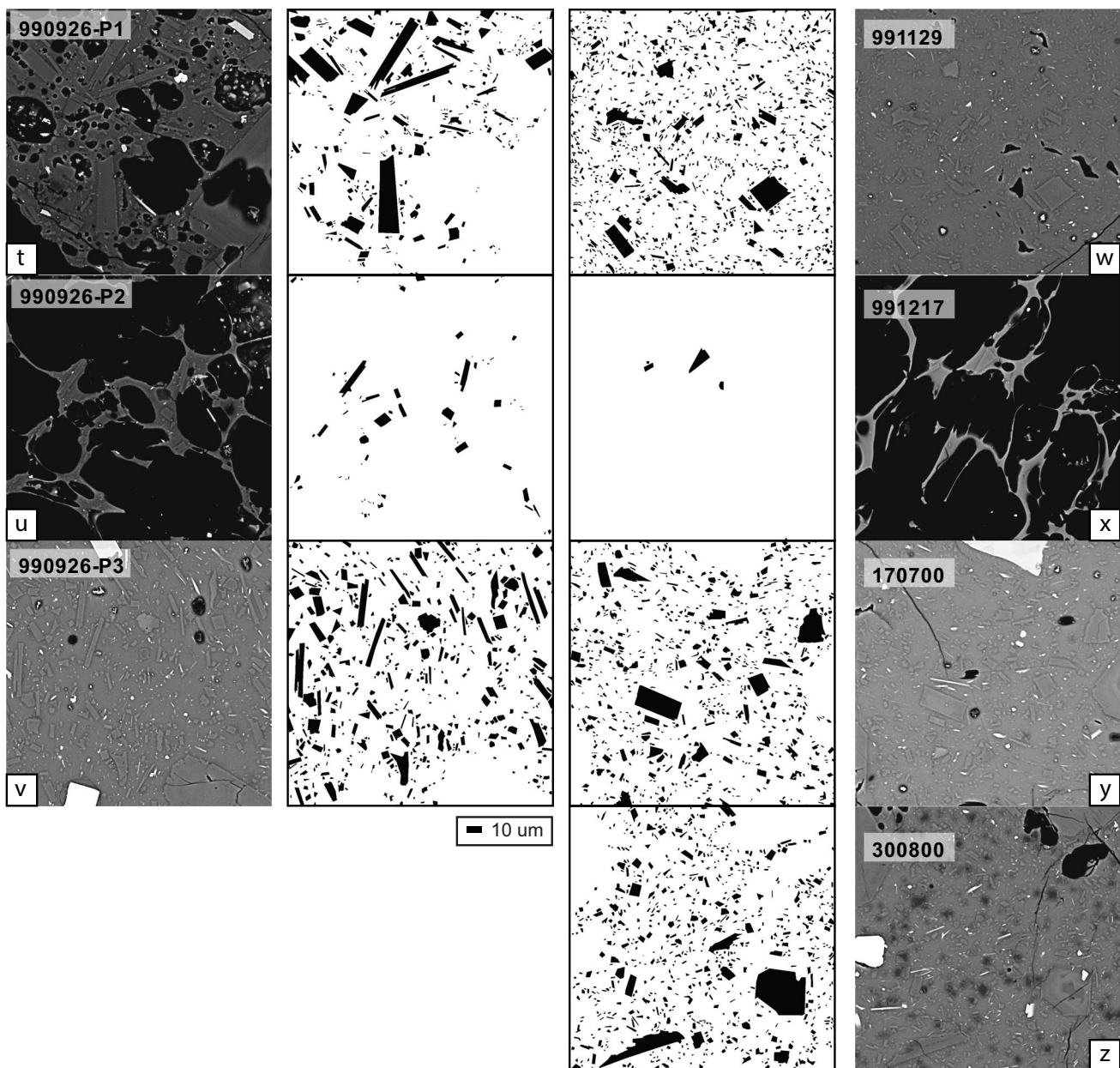
Fig. 8 (continued)

Plagioclase microlites also vary in shape, with habits that range from tabular to hopper to swallowtail. In general, elongate tabular crystal shapes are more typical of dense bombs (Fig. 9; Fig. 8a, b), tabular, swallowtail and hopper-dominated shapes are common in some breadcrusted samples (Fig. 8c–e), and low aspect ratio, acicular to tabular forms are characteristic of pumiceous and thinly breadcrusted samples (TnB; Fig. 8f, g). Tabular crystals have high modal formfactor values ($F \sim 0.7$; Fig. 9); swallowtail and hopper crystals have lower modal F (e.g., GP8 with $F \sim 0.3$) that reflects both high elongation and complex crystal boundaries. Bomb samples have best fit 3D

crystal aspect ratios (S/L from CSD slice) of 0.1–0.63 and modal F of 0.31–0.79 (Table 2). Breadcrusted samples contain elongate plagioclase microlites that extend to the lowest measured aspect ratios.

Discussion

Here, we use these compositional and textural observations to better understand the complex P-T-x path from storage to eruption, perhaps beginning in the 1980s (see Conclusions), but more significantly in 1999–2000. We start with

Table 2 Groundmass glass volatile contents and microlite textures of ballistic bombs and pyroclasts

Sample #	Sample type	wt% H_2O in bomb rind matrix glass*	ppm CO_2 in bomb rind matrix glass*	Pf (MPa)	Amphibole textures	SiO_2 phase in groundmass	Plagioclase microlite textures	Plagioclase aspect S:I:L (R^2)**	Plagioclase 2D formfactor mode
(DB) 1999-2000									
GP-17a	Dense	0.3	6	2	Intact	Yes	Tabular	1:1.4:7 (0.73)	0.72
GP-17b	Dense	0.4	9	3	Resorbed and intact	n.d.	Tabular and hopper	1:1.6:3.2 (0.87)	0.70
(FIB) 1999-2000									
GP-14	Breadcrust	0.5	b.d.	2	Resorbed and intact	Yes	Tabular and hopper	1:1.5:2.8 (0.78)	0.64
GP-3	Breadcrust	0.9	b.d.	7	Resorbed and intact	Yes	Swallowtail, hopper, acicular	1:4.5:8 (0.87)	0.42
(TkB) 1999-2000									
GP-9	Breadcrust	1.0	8	9	Resorbed and intact	Yes	Swallowtail, hopper, acicular	1:2:7 (0.67)	0.36
GP-10	Breadcrust	1.0	17	11	Intact	Yes	Tabular and hopper	1:1.7:3.2 (0.78)	0.65
GP-6	Breadcrust	1.2	10	13	Resorbed and intact	n.d.	Tabular	1:1.4:2.9 (0.79)	0.67
GP-8	Breadcrust	1.3	9	15	Intact, some with dark rims	n.d.	Swallowtail, hopper, acicular	1:3.2:8 (0.89)	0.31
GP-11	Breadcrust	1.3	14	16	Intact	n.d.	Tabular and hopper	1:1.6:3.6 (0.90)	0.67
(TnB) 1999-2000									
GP-15	Breadcrust	1.4	b.d.	16	Resorbed and intact	n.d.	Tabular	1:1.6:3 (0.89)	0.71
GP-16	Breadcrust	1.8	b.d.	25	Resorbed and intact	Yes?	Tabular	1:1.4:6 (0.79)	0.73
GP-12	Breadcrust	2.0	b.d.	31	Intact	n.d.	Tabular and hopper	1:1.8:7 (0.80)	0.72
GP-13	Breadcrust	2.1	b.d.	34	Intact	n.d.	Swallowtail, hopper, acicular	1:2.7:10 (0.58)	0.45
GP-5	Breadcrust	3.1	b.d.	65	Resorbed and intact	n.d.	Tabular	1:1.6:3.2 (0.76)	0.57

Table 2 (continued)

Date	Sample #	Sample type	wt% H_2O in bomb rind matrix glass*	ppm CO_2 in bomb rind matrix glass*	Pf (MPa)	Amphibole textures	SiO_2 phase in groundmass	Plagioclase microlite textures	Plagioclase aspect S:I:L (R^2)**	Plagioclase 2D formfactor mode
5-Oct-99	BP2	Pumice				Intact	n.d.	Tabular and hopper	1:2:10 (.72)	0.61
	P2b	Pumice				Intact	n.d.	Tabular	1:1.5:10 (.74)	0.66
	P2d	Pumice				Intact	n.d.	Swallowtail, hopper, acicular	1:1.4:9 (.69)	0.59
7-Oct-99	P3b	Pumice				Intact	n.d.	Tabular and hopper	1:1.7:4.5 (.79)	0.74
	P3d	Pumice				Intact	n.d.	Tabular and hopper	1:1.7:3.8 (.72)	0.61
26-Sept-99	990926-P1	Pumice				Intact	Yes	Tabular and hopper	1:1.4:8 (.64)	0.60
	990926-P2	Pumice				Intact	Yes	Tabular and hopper	1:1.25:7 (.66)	0.71
	990926-P3	Dense				Resorbed and intact	Yes	Tabular	1:1.15:1.6 (.83)	0.76
29-Nov-99	991129	Dense					n.d.	Tabular	1:1.5:2.9 (.82)	0.79
17-Dec-99	991217	Pumice				Intact	n.d.	Tabular	1:1.3:2.4 (.53)	0.76
17-Jul-00	170700	Dense				Resorbed and intact	Yes	Tabular	1:1.8:2.5 (.83)	0.73
30-Aug-00	300800	Dense				Breakdown (2–4 um)	Yes	Tabular	1:1.6:2.9	0.72

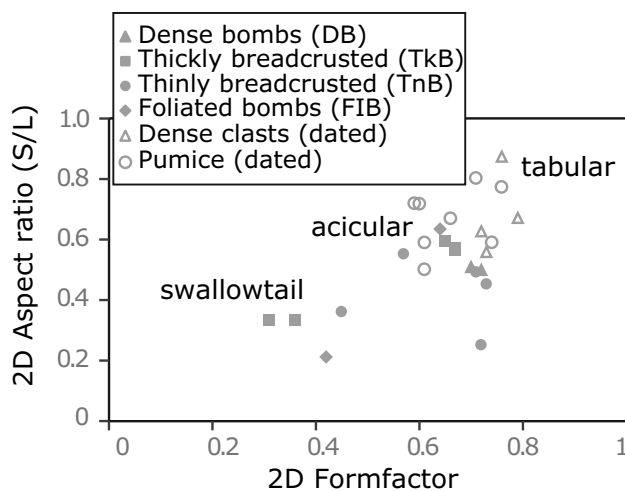|	Sample #	Sample type	Plagioclase 2D aspect ratio mode	Plagioclase fabric***	Plagioclase microlite crystallinity (%)	Mafic microlite crystallinity (%)	3D S/L	Plagioclase log N_a (mm^{-2})	Plagioclase log N_T steep (mm^{-3})***
(DB) 1999-2000	GP-17a	Dense	0.50	0.41	9	2.3	0.14	3.48	5.92
	GP-17b	Dense	0.51	0.19	12	1.4	0.31	4.72	8.16
(FIB) 1999-2000	GP-14	Breadcrust	0.63	0.04	8	1.1	0.36	4.37	7.74
	GP-3	Breadcrust	0.21	0.6	14	3.4	0.13	4.51	7.99
(TkB) 1999-2000	GP-9	Breadcrust	0.33	0.1	17	1.2	0.14	4.94	7.26
	GP-10	Breadcrust	0.59	0.23	16	1.3	0.31	4.44	7.69
	GP-6	Breadcrust	0.57	0.12	16	1.1	0.34	4.22	7.39
	GP-8	Breadcrust	0.33	0.17	19	0.6	0.13	4.53	7.17
	GP-11	Breadcrust	0.56	0.24	13	0.7	0.13	4.59	7.78

Table 2 (continued)

	Sample #	Sample type	Plagioclase 2D aspect ratio mode	Plagioclase fabric***	Plagioclase microlite crystallinity (%)	Mafic microlite crystallinity (%)	3D S/L	Plagioclase log N_a (mm^{-2})	Plagioclase log N_T steep (mm^{-3})***
(TnB) 1999-2000	GP-15	Breadcrust	0.49	0.22	12	1.9	0.16	4.38	7.68
	GP-16	Breadcrust	0.45	0.09	12	1.1	0.17	4.41	7.41
	GP-12	Breadcrust	0.25	0.05	15	1.3	0.14	4.54	6.96
	GP-13	Breadcrust	0.36	0.11	9	0.6	0.10	4.47	7.62
	GP-5	Breadcrust	0.55	0.14	12	2.1	0.31	4.39	7.69
5-Oct-99	BP2	Pumice	0.50	0.13	17	1.2	0.10	4.49	7.30
	P2b	Pumice	0.67	0.12	23	2.4	0.10	4.17	6.80
	P2d	Pumice	0.71	0.23	10	n.d.	0.11	4.67	7.56
7-Oct-99	P3b	Pumice	0.59	0.18	21	n.d.	0.22	4.33	7.60
	P3d	Pumice	0.59	0.07	14	n.d.	0.26	4.69	7.79
26-Sept-99	990926-P1	Pumice	0.71	0.15	22	1.7	0.13	4.28	7.79
	990926-P2	Pumice	0.80	0.4	13	4.4	0.14	3.95	6.47
	990926-P3	Dense	0.87	0.11	16	2.9	0.63	4.26	6.89
29-Nov-99	991129	Dense	0.67	0.12	13	0.4	0.34	4.54	7.92
17-Dec-99	991217	Pumice	0.77	0.11	4	n.d.	0.42	3.22	6.02
17-Jul-00	170700	Dense	0.56	0.29	16	1.1	0.40	4.39	7.60
30-Aug-00	300800	Dense	0.63	0.09	14	2.4	0.34	4.41	7.62

*From FTIR spectroscopy (Wright et al., 2007)

** S (short); I (intermediate); L (long) axes from CSD slice (Morgan and Jerram 2006)

*** From CSD corrections (Higgins 2000)

Fig. 9 Modal plagioclase microlite two-dimensional (2D) formfactor versus 2D aspect ratio for all samples. Note that variation in crystal shape correlates with difference in measures of formfactor and aspect ratio

an estimation of temperature and oxygen fugacity conditions from co-existing oxide pairs in erupted samples. We use dissolved H_2O and CO_2 contents to constrain minimum crystallization pressures and then use groundmass glass compositions and amphibole textures to frame discussion of decompression and shallow storage that drives microlite crystallization. Finally, we demonstrate evidence for repeated cycles of decompression, repressurization, and gas streaming as preserved in high microlite number densities, variable microlite crystallinities, oscillatory-zoned plagioclase, and measurable groundmass CO_2. We conclude with an eruption model that integrates all of these observations with seismic data and observational records of explosive eruptions that punctuate protracted periods of dome growth.

Temperature and oxygen fugacity

We use the Mg/Mn partitioning test for equilibrium of Bacon and Hirschmann (1988) to evaluate degree of equilibrium of oxide pairs. We calculate resulting temperatures using both the geothermometer of Andersen and Lindsley (1988) with the recalculation of Stormer (1983; using ILMAT, Lepage 2003) and the geothermometer of Ghiorso and Evans (2008). Temperatures and oxygen fugacities calculated using the former are generally higher than those using the latter, although relative variations in temperature and oxygen fugacity are consistent between the two thermometers (Table 7SM). Here, we specify only the results of Ghiorso and Evans (2008), which are reported to be more accurate for magmas that equilibrated under conditions more oxidizing than the nickel–nickel-oxide buffer (NNO). Only three

pairs pass the Bacon and Hirschmann (1988) equilibrium test although another three are very close to equilibrium (Table 7SM). The average temperature of the three pairs that pass the equilibrium test is 840 °C. All oxide pairs indicate equilibrium within 1.2–1.5 log units above the NNO oxidation buffer (Fig. 4SM). Equilibrium temperatures range from 805 to 905 °C; the lowest temperature pair is found in a dense bomb, the intermediate temperature pairs are found in thickly breadcrusted bombs, and the highest temperature pairs (just outside of the Mg/Mn partitioning bounds) are found in foliated breadcrust bombs.

Storage depth

H_2O contents of 2.7–4.6 wt% measured by FTIR overlap with calculations of H_2O content using the plagioclase-melt hygrometer of Waters and Lange (2015) of 3.8 to 4.5 wt% H_2O, using an equilibration temperature of 840 °C (Fig. 3, Table 7SM). We use the volatile saturation model of Newman and Lowenstern (2002) to calculate saturation pressures from these measured melt inclusion volatile concentrations and to calculate H_2O and CO_2 solubilities at 840 °C (Fig. 3). Melt inclusion saturation pressures fall between 69 and 168 MPa, or equilibration depths between 2.8 and 6.8 km (using an overlying magma density of 2500 kg/m³). The lower end of this range overlaps with equilibration pressures/depths calculated for volatiles dissolved in groundmass glass from the most vesicular breadcrust bomb (Wright et al. 2007). The upper end of the range overlaps with geobarometry estimates of amphibole in 1999 dome rocks from Garcia-Aristizabal et al. (2008) of 100–300 MPa or 4–12 km below the summit. This correspondence is reassuring given the lack of measurement of CO_2 within vapor bubbles in this study, especially given the recognition that 40–90% of CO_2 can be trapped in bubbles (Moore et al. 2015). Based upon these estimates, we infer that magma crystallized over a range of depths that extended to at least ~7 km beneath the summit.

Melt inclusion CO_2 contents range from 19 to 310 ppm and can be used in conjunction with H_2O contents to model exsolution and degassing in the system. Here, we use VolatileCalc 2.0 (Newman and Lowenstern 2002) to model degassing (and possible regassing) from a rhyolitic melt containing 4.6 wt% H_2O and 500 ppm CO_2 (saturation pressure of ~200 MPa). This composition matches the maximum H_2O content measured in melt inclusions and uses a slightly higher CO_2 concentration of 500 ppm to account for potential unmeasured CO_2 in melt inclusion vapor bubbles, consistent with the maximum CO_2 measured in some other arc rhyolitic systems (Wallace 2005).

Variations in H_2O and CO_2 content are inconsistent with simple open or closed system degassing models if our starting composition is accurate (steep, solid gray lines on Fig. 3), which predict extensive CO_2 loss prior to H_2O

Table 3 Phenocryst and groundmass proportions of dense and breadcrusted bombs, all values are percentages of the solid fraction (reported on a vesicle-free basis)

Phenocryst point count data

Sample #	GP-17a	GP-17b	GP-8	GP-9	GP-10	GP-11	GP-6	GP-3	GP-14	GP-13	GP-15	GP-12	GP-16	GP-5
Crystallinity	46.7	45.2	40.1	50.5	41.5	40.7	39.6	41.9	39.1	43.3	44.5	36.6	38.1	30.9
Plagioclase	32.0	32.5	28.8	38.5	31.6	33.0	28.6	30.5	31.0	31.7	32.5	27.3	28.4	23.2
Hornblende	11.1	8.2	9.6	7.3	7.5	6.5	7.2	6.8	5.5	6.4	6.7	4.3	5.5	4.5
Oxides	2.1	2.4	1.2	1.5	1.6	0.2	2.0	2.2	1.4	2.1	2.0	2.2	2.4	1.0
Orthopyroxene	1.5	2.0	0.6	3.2	0.8	1.0	1.8	2.4	1.2	3.1	3.3	2.8	1.8	2.3
Groundmass	53.3	54.8	59.9	49.5	58.5	59.3	60.4	58.1	60.9	56.7	55.5	63.4	61.9	69.1

All point count values listed as % of total, normalized to 100% on a vesicle-free basis

exsolution. Instead, CO_2 contents remain elevated at lower H_2O contents. H_2O-CO_2 trends that deviate from predictions of open and closed system degassing have been variously explained by closed system degassing in the presence of an external H_2O and CO_2-bearing fluid phase (Rust et al. 2004; Spilliaert et al. 2006; Blundy et al. 2010; modeled here with shallow dashed lines in Fig. 3) or post-entrapment diffusive H loss from melt inclusions (Gaetani et al. 2012; Lloyd et al. 2013). Post entrapment diffusive H loss would not explain the presence of CO_2 in groundmass glass of Guagua Pichincha breadcrust bombs. For this reason, we favor the former interpretation, whereby CO_2-rich gas exsolved from magma at depth equilibrates with shallow magma en route to the surface. Modeled closed system degassing paths with 1 and 2 wt% vapor are shown in dashed lines in Fig 3. No single model fits all of the melt inclusion and groundmass glass data. We suggest that this variation records spatial variability in gas migration pathways.

Within this framework, variation in the estimated pressures of groundmass glass and melt inclusions (to maximum 168 MPa or 6.8-km depth) likely reflects continued crystallization (and melt inclusion entrapment, as suggested by the presence of different melt inclusion generations along the numerous compositional zone boundaries in plagioclase and clinopyroxene) during ascent. The slightly higher maximum and minimum H_2O contents in the 5 October pumice clasts relative to those measured from later eruptions is permissive of a slight shallowing of the storage zone from which magma was extracted between 5 and 7 October or could be related to the local effect of decompression in the reservoir system due to its partial replenishment following the first eruptive event.

H₂O-exsolution-induced crystallization

As magma ascends and decompresses within ascent pathways (including the shallow conduit), volatiles exsolve, effectively undercooling the magma (i.e., increasing the melt's liquidus temperature) and inducing crystallization of the melt. Evidence for the extent to which this occurred during the Guagua Pichincha eruptions is provided by the abundance and composition of groundmass crystal phases.

Table 4 End member plagioclase microlite and phenocryst compositions. Oxide compositions are shown in wt%

Clast texture	Sample		SiO2	Al2O3	FeO	CaO	Na2O	K2O	Total	Ab	An	Or
(DB)	GP17a	Microlite	54.5	28.4	0.5	10.9	5.3	0.3	100.0	45.9	52.5	1.7
		Microlite	58.5	25.5	0.7	8.0	6.7	0.4	99.9	59.0	39.0	2.1
	GP17b	Microlite	56.0	27.5	0.4	9.3	6.2	0.3	99.8	53.9	44.2	1.9
		Microlite	57.9	26.1	0.3	7.7	7.4	0.4	100.0	61.8	35.7	2.5
(TkB)	GP6	Microlite	55.4	27.8	0.4	10.3	5.7	0.2	99.9	49.2	49.5	1.3
		microlite	56.9	26.9	0.4	8.6	6.6	0.3	99.7	57.1	41.1	1.8
	GP8	phenocryst	57.6	26.9	0.3	8.0	6.8	0.3	100.0	59.5	38.7	1.8
		phenocryst	50.0	32.4	0.6	13.3	3.5	0.2	100.0	31.6	67.1	1.3
(ThB)	GP5b	microlite	56.9	26.7	0.5	8.7	6.6	0.3	99.8	56.8	41.3	1.8
		microlite	56.9	26.9	0.4	8.5	6.7	0.3	99.7	57.7	40.5	1.9
pumice	7-October	phenocryst	58.3	26.5	0.3	7.7	6.8	0.4	100.0	60.0	37.7	2.4
		phenocryst	50.5	31.5	0.4	13.8	3.6	0.2	100.0	31.5	67.3	1.1
pumice	5-October	phenocryst	60.1	25.3	0.4	6.5	7.2	0.5	100.0	64.6	32.4	3.0
		phenocryst	50.6	31.3	0.7	13.7	3.5	0.2	100.0	31.4	67.3	1.3
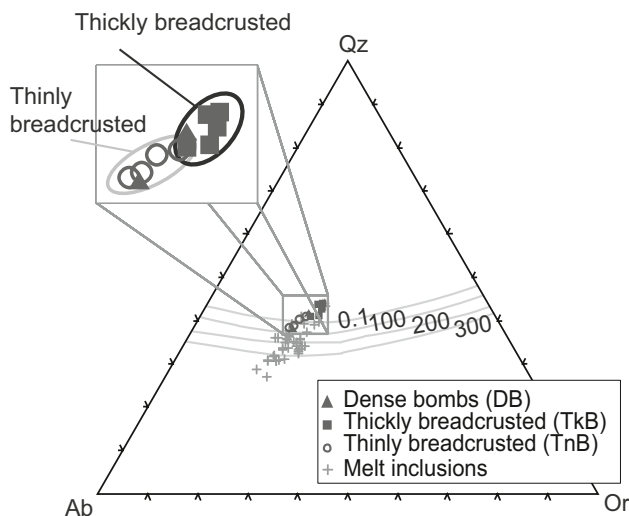
Fig. 10 Groundmass glass compositions of bombs in this study plotted on the haplogranitic ternary using the correction scheme of Blundy and Cashman (2001; Quartz-feldspar cotectics (in MPa) for the Qz-Ab-Or system from Brugger et al. 2003). Only analyses with less than 1 wt% normative corundum were used in this plot

A simple mass balance calculation that treats K_2O as incompatible suggests that overall sample crystallinities vary from 44 to 54%. When phenocryst crystallinities (Table 3) are subtracted from the total crystallinities, groundmass crystallization of 0 to 30% is implied, an estimate that is consistent with calculations from image analysis of bombs (9–20% total groundmass crystallinity; Table 2).

The extent of crystallization can be related to decompression by projection of groundmass glass compositions on the haplogranite ternary diagram (Qz-Ab-Or), using the correction scheme of Blundy and Cashman (2001; Fig. 10). This projection scheme enables comparison of rhyolite melt compositions with experimentally derived H_2O-saturated crystallization paths and quartz-feldspar cotectic pressures and temperatures (Cashman and Blundy 2000; Blundy and Cashman 2001; Brugger et al. 2003). Melt compositions that lie along a single compositional trend are consistent with ascent from high to low pressure, forming a single liquid line of descent. Melt inclusion and groundmass glass compositions of Guagua Pichincha melts do not fall along a single compositional trend, however, suggesting that the melt evolution history is neither simple nor homogeneous among different samples (Fig. 4; cf. Cashman and Edmonds 2019). The range of melt inclusion compositions is consistent, however, with entrapment and isolation at different locations along the decompression path (Blundy and Cashman 2005). In contrast, groundmass glass compositions of all bombs from Guagua Pichincha record equilibration at

shallow levels, consistent with inferences from preserved volatile contents (Wright et al. 2007).

Groundmass glass compositions are also distinctive for individual bomb types, with thinly breadcrusted (TnB) glasses less evolved than those of thickly breadcrusted (TkB) and Dense (DB) clasts (Fig. 10). These compositional variations confirm the relative stratigraphy defined by the measured volatile contents and indicate sufficient residence time at shallow levels for crystallization to follow degassing. Absolute equilibration pressures can be estimated only for samples containing a groundmass silica phase, and then only if equilibrium was attained. Quartz precipitation in high silica rhyolite melt requires $P < \sim150$ MPa (depending on temperature) and appears to require residence times of hours to days (Cashman and McConnell 2005). At large degrees of undercooling, however, magmas may overshoot low pressure quartz-feldspar cotectics due to the restricted kinetics of quartz precipitation reactions, while feldspar continues to precipitate (Blundy and Cashman 2001; Martel and Schmidt 2003; Couch et al. 2003). An overabundance of normative Qz' suggests that quartz is supersaturated in the melt. Indeed, groundmass glass compositions of most quartz-bearing Guagua Pichincha bombs (DB, TkB) plot on the quartz side of the estimated 1-atm quartz-feldspar cotectic. Although equilibration pressure cannot be determined from major element compositions plotted on a haplogranite ternary, H_2O contents within groundmass glass from the most vesicular breadcrust bombs limit equilibration pressure to a maximum of 69 MPa (Wright et al. 2007).

Breakdown of hornblende may provide additional information on conditions of decompression and cooling (Rutherford and Hill 1993; Browne and Gardner 2006; Cashman and McConnell 2005). Under isothermal conditions at 900 °C and constant decompression, hornblende will not develop reaction rims if rates of magma ascent exceed ~ 2 cm/s (Rutherford and Devine 2003). This condition translates to minimum decompression rates of $\sim 5\times10^{-4}$ MPa/s for a bulk magma density of 2500 kg/m^3. Non-linear decompression paths or lower temperatures, however, can shift these values to lower minimum ascent rates or longer residence times (Rutherford and Devine 2003; Browne and Gardner 2006). Annealing at $P = 20$ MPa (appropriate to many of the Guagua Pichincha samples) requires 7–8 days for hornblende breakdown to begin (Rutherford and Hill 1993; Browne and Gardner 2006). Guagua Pichincha samples lack hornblende breakdown textures in either the explosive or effusive products, with the one exception being the final dome sample from 2000, which has the longest preceding repose time. Hornblende textures are thus consistent with the $\leq$ 7-day repose interval preceding most Guagua Pichincha Vulcanian eruptions, at least for the shallow-sourced samples.

## Textural evidence for decompression and repressurization

Textural characterization of crystals in volcanic samples has been used to track decompression and degassing-induced crystallization histories through both comparison with experimental studies (Geschwind and Rutherford 1995; Hammer and Rutherford 2002; Martel and Schmidt 2003; Couch et al. 2003; Shea and Hammer 2013; Riker et al. 2015; Lindoo and Cashman 2021) and examination of well documented natural samples (e.g., Cashman 1988, Wolf and Eichelberger 1997; Hammer et al. 1999; Cashman and Blundy 2000; Martel et al. 2000; Cashman and McConnell 2005; Pardo et al. 2014; Bain et al. 2019). Studies of natural systems, however, do not present such a clear story (Cashman et al. 2020).

Microlite crystallization experiments have explored a range of H_2O exsolution rates, mechanisms (single-step, continuous, and multi-step decompression; reported by Geschwind and Rutherford 1995; Couch et al. 2003; Brugger and Hammer 2010; Martel 2012; Riker et al. 2015; Befus and Andrews 2018), and final pressures (P_f; Hammer and Rutherford 2002; Martel and Schmidt 2003; Couch et al. 2003; Suzuki et al. 2007; Cichy et al. 2011; Andrews and Gardner 2010; Brugger and Hammer 2010; Mollard et al. 2012; Shea and Hammer 2013). Put simply, the rate of H_2O exsolution determines the effective undercooling, which controls the relations between nucleation and growth rates of plagioclase microlites in a given melt (Cashman and Blundy 2000; Toramaru et al. 2008). Where H_2O exsolution is driven by decompression, maximum plagioclase microlite number density should correlate with magma decompression rate and thereby with eruption style (Cassidy et al. 2018). Additionally, cooling rate controls textural maturation (Vetere et al. 2013; Shea and Hammer 2013) and crystallization duration controls abundance (approach to equilibrium). To assess the extent to which these correlations hold in natural samples in general, we compared Guagua Pichincha plagioclase textural data with previously published data for pyroclasts with intermediate bulk compositions and rhyolitic melt compositions. When plotted as N_a (or N_v, volumetric number density) versus microlite crystallinity (Fig. 12a, b), these data show more than a 3 order-of-magnitude variation in N_a (more than 4 orders of magnitude for N_v) and no apparent correlation with microlite crystallinity except in pyroclasts from closely spaced eruptions that immediately preceded the climactic eruption of Pinatubo in 1991 (Hammer et al. 1999) or, to a minor extent, in samples from the 1986–1994 dome eruptions of Merapi (Hammer et al. 2000). The 1995–2010 eruptive episode of Soufriere Hills volcano shows the greatest variation within an eruption sequence, while samples from the 1991–1995 low

explosivity eruption of Unzen (both dome and feeder dike) show the least variation. More generally, the products of dome-forming and Vulcanian eruptions have lower microlite number densities than those from Subplinian and Plinian eruptions (including Pinatubo and Mt. Pelee). Samples from Guagua Pichincha have intermediate number densities that are similar to those from Vulcanian and some dome collapse events at Soufriere Hills volcano, although with higher number densities and lower microlite crystallinities than most Vulcanian and dome-forming eruption samples.

Several features of the rocks raise questions about simple interpretations of groundmass textures (Fig. 11c–e). As expected, maximum microlite crystallinities roughly correlate with repose interval prior to eruption (Fig. 11c; although samples from Shinmoedake volcano are an exception), supporting a model of decompression in response to preceding eruptions in a sequence. The wide variation for individual eruptions seen in Fig. 12c, in contrast, reflects the pulsatory nature of Vulcanian eruptions, during which sudden decompression rapidly evacuates much of the shallow conduit. The resulting pyroclasts include magma that resided, and may have equilibrated, at a range of pressures (Cashman and McConnell 2005; Clarke et al. 2007; Wright et al. 2007; Gabellini et al. 2022). We invoke the same explanation for the lack of correlation between number density and either the VEI or the maximum column height (eruption intensity) of the pyroclast-forming eruption at Guagua Pichincha (Fig. 12d, e). This limited analysis highlights the nature of pulsatory eruptive activity, particularly the condition that, unlike steady eruptive activity, rates of magma ascent in the conduit are not directly correlated with conditions of eruption. This being the case, what information can we obtain from textural studies?

A direct comparison of experimental and volcanic data shows that decompression experiments have failed to replicate the highest observed plagioclase number densities (Fig. 11a, b; Cashman 2020). Importantly, most experiments use only H_2O as the volatile phase, and assume uni-directional pressure paths. Only two experimental studies address the additional features that we suggest may be important in determining the final groundmass textures of the Guagua Pichincha samples, namely (1) re-equilibration with a CO_2 rich volatile phase (Riker et al. 2015) and (2) decompression/recompression cycling; Lindoo and Cashman 2021). The former shows that reducing the melt H_2O content by introducing CO_2 increases plagioclase crystallization rates over the H_2O-only experiments; the latter shows that pressure cycling acts to disrupt complex dendritic crystal networks to produce high number densities of crystals via a form of secondary nucleation. Although there does not appear to be a direct correlation between dissolved CO_2 in the groundmass melt and anomalously high plagioclase
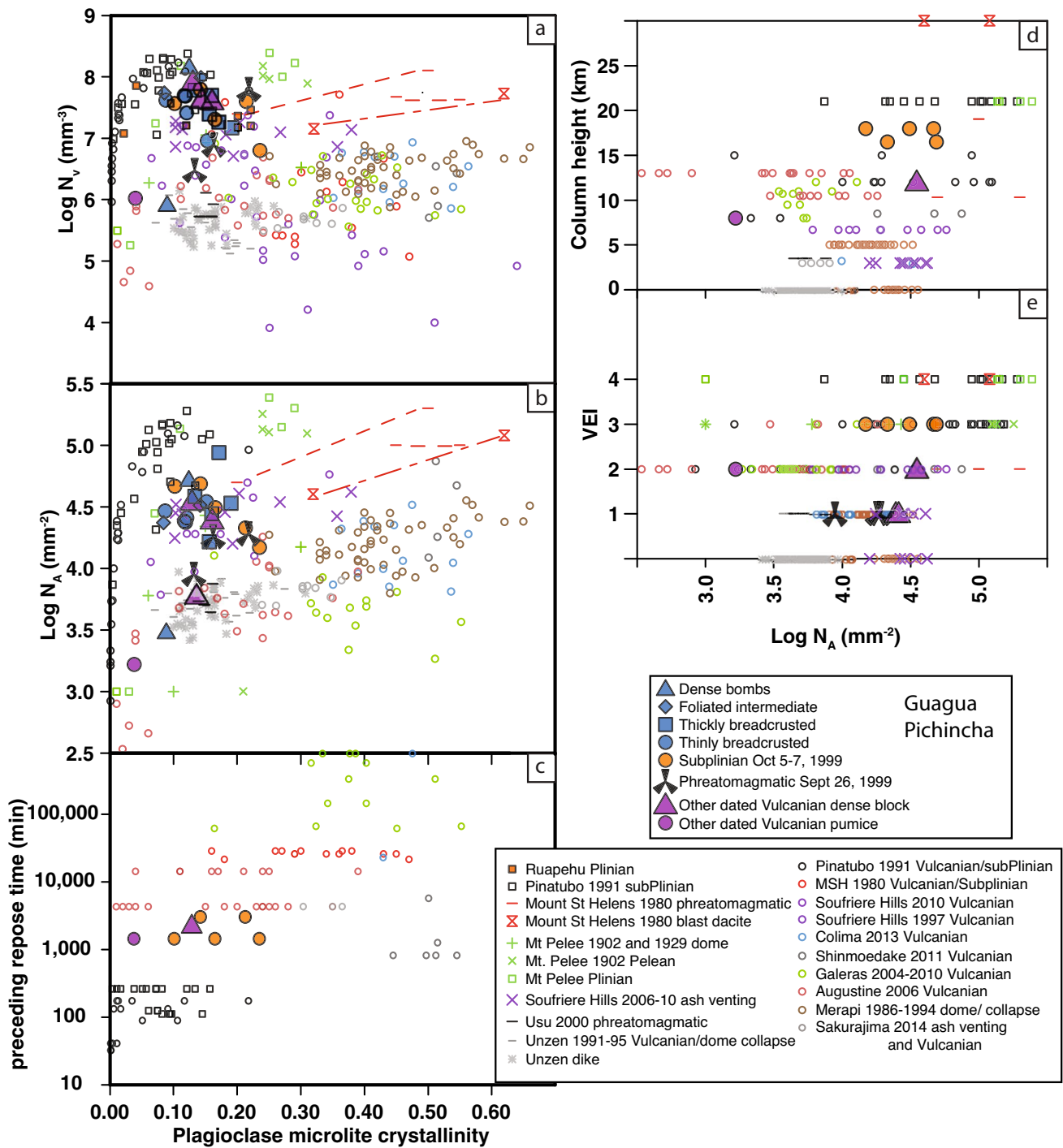
Fig. 11 Groundmass plagioclase crystallinity versus volumetric and areal number density of Guagua Pichincha samples. Plagioclase microlite textural data from other andesitic to dacitic natural samples (with rhyolitic groundmass glass compositions) are plotted for comparison (Ruapehu, Pardo et al. 2014; Pinatubo 1991, Hammer et al. 1999; Mount St. Helens 1980, Cashman and Hoblitt 2004 and Cashman and McConnell 2005; Mt. Pelee 1902 and 1929, Martel and Poussineau 2007; Soufriere Hills 1997, Clarke et al. 2007; Soufriere Hills 2006-2010, Murch and Cole 2019; Colima 2013, Cassidy et al. 2015; Shinmoedake 2011, Suzuki et al. 2018; Galeras 2004-2010, Bain et al. 2019 and 2021; Augustine 2006, Benage et al. 2021; Merapi 186-1994, Hammer et al. 2000; Sakurajima 2014, Gabellini et al. 2022; Usu 2000, Suzuki et al. 2007; Unzen 1991-1995 and dikes, Noguchi et al. 2008). Dashed red lines extend across the ranges of crystallinity and number density values reported by Cashman and Hoblitt (2004) for Mount St. Helens pyroclasts
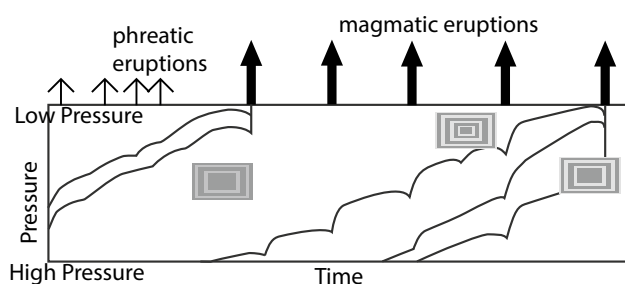
Fig. 12 Cartoon schematic of pressure-time paths inferred for eruptive products from sequential eruptions at Guagua Pichincha. Pressure does not correlate directly with depth here due to the ability for overpressure to build as the conduit densifies and seals. Note that pressure cycling may produce oscillatory zones in plagioclase crystals, as in Fig. 5. Hypothetical variations in oscillatory zonation are shown next to pressure-time paths

number densities, it is interesting that samples with high N_a at Pinatubo and Mount St. Helens are from pre-climactic sequences that involved multiple small eruptions (cycling of recompression-decompression events).

How does this assessment help us to interpret the groundmass textures of Guagua Pichincha samples? The limitations described above, together with a lack of experiments that replicate the eruption conditions at Guagua Pichincha (inferred rapid decompression to pressures of ≤ ~70MPa followed by slow decompression to shallower pressure, probably accompanied by repressurization and variable amounts of CO_2 fluxing), limit the extent to which Guagua Pichincha textures can be interpreted quantitatively. Nonetheless, the combination of groundmass crystal textures, oscillatory zoned plagioclase, and volatile data strongly suggest that (1) Guagua Pichincha magma was repeatedly staged at variable but shallow levels prior to eruption, (2) intra-eruptive decompression and degassing occurred rapidly in response to the preceding eruption, but decreased as material outgassed and densified (as interpreted at Soufriere Hills, Edmonds et al. 2003), and (3) streaming of CO_2-rich gas could have increased rates of crystallization above those imposed by decompression alone (e.g., Riker et al. 2015). Rapid crystallization due to decompression is further supported by the abundance of swallowtail and hopper crystal morphologies in many of the samples (e.g., Hammer and Rutherford 2002), while pressure cycling is required by the episodic Vulcanian activity.

An exception to the above discussion is DB sample GP17a, which has the lowest H_2O in groundmass glass (lowest equilibration pressure) but also exhibits anomalously low crystallinity and plagioclase number densities with relatively large crystal sizes; the pumiceous sample from 17 December 1999 (erupted after the highest effusion rate period of the sequence; Table 1) has similar characteristics. We interpret

these features to reflect rapid syn-eruptive degassing followed by limited crystallization because of high melt viscosities, as seen in the lowest pressure (5 MPa) experiments of Hammer and Rutherford (2002). Lack of equilibrium in this low-pressure experimental sample is confirmed by a groundmass glass composition that plots near higher pressure cotectics on the haplogranite ternary (Fig. 10; see also Martel and Schmidt 2003).

To summarize, groundmass textures of Guagua Pichincha samples, specifically, and samples from silicic pulsatory eruptions, in general, do not fit predictions based on either steady or non-steady uni-directional decompression paths. Instead, they and the oscillatory zones found in plagioclase rims record (1) sudden evacuation of magma residing at different levels in the shallow conduit and (2) inter-eruptive repose periods marked by time-varying rates of degassing (+ volatile fluxing) and re-pressurization (mirrored by time-varying rates of summit deflation and then inflation; Garcia-Aristizabal et al. 2007). Critically, this means that, in contrast to steady eruptions, the magma decompression/recompression history recorded in the groundmass textures of the clasts may be *decoupled* from the dynamics of final, syn-eruptive magma ascent. For this reason, the final decompression is only part of the story recorded in plagioclase groundmass and phenocryst rim textures. Additional information is included, however, in the volatiles dissolved within the groundmass melt. We note that elevated CO_2 in groundmass glass is not unique to Guagua Pichincha but is also observed in groundmass glass from breadcrust bombs formed during pulsatory eruptions at Galeras and Mount St. Helens (Bain et al. 2019; Blundy et al. 2010); we suspect that the same is true for other pulsatory eruptions where the volatile content of groundmass glass has not been analyzed.

Variations in the number of oscillatory zones in plagioclase phenocrysts further indicate that decompression, degassing, and repressurization paths varied through time in the eruption sequence. Samples from the first (phreato) magmatic eruption on 26 September contain very few oscillatory zones, consistent with decompression accompanying relatively modest ascent rates, punctuated by decompression-recompression steps associated with the limited number of precursory phreatic events (Fig. 12). Samples erupted on 5 October similarly show a limited number of zones due to their eruption early in the sequence. Oscillatory zones in samples from the subsequent activity are more numerous and overlap those in thinly breadcrusted (TnB) samples and dense (DB) samples, consistent with effective quench at (multiple) shallow levels (and low overall crystallinity). thickly breadcrusted (TkB) and foliated intermediate (FIB) samples have the highest number of zones, are similar to each other, and are interpreted to originate from shallow in the conduit (although not so shallow as to stop growth as in dense DB samples).

Conclusions

We combine chemical and textural information to create a holistic model of eruptions in the 1999–2000 Guagua Pichincha eruption sequence. Melt inclusions show a range of H_2O and CO_2 concentrations that may reflect closed system degassing in the presence of an external fluid. Plagioclase microlite number densities, size distributions, shapes, oscillatory zonation, and presence of silica-phase precipitation indicate multiple decompression/recompression steps preceding eruption as magma stalled within shallow crustal pathways beneath the vent. In addition, CO_2-bearing groundmass glass provides evidence for equilibration with magmatic gas from depth during inter-eruptive intervals while the system repressurized. Shallow staging was accompanied by crystallization with sufficient shallow residence times to allow silica to precipitate, but not long enough for hornblende breakdown rims to form. Together these constraints limit shallow residence duration, consistent with repose intervals between dome destruction events averaging ~7 days.

These observations inform our conceptual model of the Guagua Pichincha magmatic system and the sequence of events leading to repeated eruptions in 1999–2000.

1. Magma storage (growth of equilibrium phenocryst assemblage) at >3 to 7 km below the crater floor, as indicated by melt inclusion saturation pressures that are themselves minima due to lack of accounting for CO_2 in melt inclusion bubbles. This depth range is consistent with, but not as extensive as, an amphibole geobarometry depth range of 4–12 km (Garcia-Aristizabal et al. 2007) and VT hypocenter locations that extend to a maximum of 14 km below the crater floor.

2. Magma ascent and/or degassing from this reservoir activates faults distal to the magma (due to either increase of pore pressure in groundwater, cf. White and McCausland (2016), or stress loading on tectonic faults distal from magmatic intrusion). Distal VT (dVT) seismicity occurred on a pre-existing splay of the Romeral Fault Zone about 15 km away from the volcano at 14-km depth. The earliest signs of magma ascent occurred as early as 1981, when seismicity felt in Quito in August 1981 was followed only 3 days later by the first phreatic eruption at Guagua Pichincha in over 100 years (Global Volcanism Program 1981). By late 1997 to early 1998, dVT seismicity (to maximum magnitude of 4.0; Legrand et al. 2002; White and McCausland 2016) increased in frequency, waxing and waning in close relationship to phreatic activity at the volcano and peaking at times of notable phreatic eruptions, although it did not migrate progressively closer to the volcano through time.

3. Shallow magma ascent accompanied by dVT swarms detected in September 1998 and again in January to March 1999 (Fig. 2), which were followed by increases in hydrothermal activity, increasing phreatic eruptions, and by the new appearance of shallow tremor. Strong tremor lasted days to weeks from March to May 1999, accompanied by increasing, vapor-rich phreatic eruptions and a swarm of proximal VT earthquakes. Another swarm occurred in June 1999 (with fewer, but larger magnitude events and ash-rich eruptions). Then, from 8 to 24 September 1999, VT focal depths shallowed to 2 km below the surface (Garcia-Aristizabal et al. 2007) causing shallow deformation detected with a near-summit tiltmeter and shallow LP seismicity. Magma surfaced on 26 September with ash eruptions and then created the first dome on ~28 September. Plagioclase phenocrysts in ash samples show very limited oscillatory rim growth, suggesting that the preceding phreatic activity did little to influence the shallow magma. Inflationary tilt signals prior to explosive eruptions within the ensuing sequence have been interpreted to reflect accumulation of pressure beneath a rigid dome cap (Garcia-Aristizabal et al. 2007). Deflation then accompanied many of the subsequent explosions (Garcia-Aristizabal et al. 2007). Shallow ascent is interpreted to have occurred within a network of dikes at <3-km depth, coincident with a prolate low velocity seismic anomaly that extends from 1 to 3 km beneath the crater floor (Garcia-Aristizabal et al. 2007) and with most VT seismicity, for which relocated hypocenters form subvertical alignment to ~ 2-km depth (Garcia-Aristizabal et al. 2007).

4. Repeating cycles of explosive magmatic eruptions followed by dome growth and subsequent destruction (Fig. 12): in eight consecutive cycles, magma slowly ascended toward the surface, filling and staging within shallow dikes at 0–3 km. Degassing accompanied magma ascent (producing low H_2O contents in breadcrust rinds), causing microlite crystallization and forming oscillatory rims on the plagioclase phenocrysts; the latter provide a rough estimate of the relative magma residence time within the conduit prior to being expelled in an eruption. Associated outgassing (as evidenced by low breadcrust rind porosities, Wright et al. 2007) contributed to plug formation beneath the growing dome (as modeled by Schneider et al. 2012), where the closed system degassing trends of melt inclusion volatile contents suggest that degassing outpaced outgassing rates. The system repressurized due to continued degassing of shallow magma beneath a low-permeability cap and the additional contribution of gas streaming from depth (causing elevated CO_2 contents in breadcrust rind groundmass

glass). LP swarms during dome extrusion may signal this pressure accumulation (cf. changing character of LPs at Galeras, Torres et al. 2021). In general, LP swarms began with irregular spacing, but became more closely spaced through time until merging into tremor (Garcia-Aristizabal et al. 2007) and leading to pulses of dome growth, which sometimes culminated in explosion and dome collapse (Villagómez 2000).

References

Andersen DJ, Lindsley DH (1988) Internally consistent solution models for Fe-Mg-Mn-Ti oxides; Fe-Ti oxides. Amer. Mineral. 73(7-8):714–726

Andrews BJ, Gardner JE (2010) Effects of caldera collapse on conduit dimensions and magma decompression rate: an example from the 1800 14C yr BP eruption of Ksudach volcano, Kamchatka, Russia. J Volcanol Geotherm Res 198:205–216

Bacon CR, Hirschmann MM (1988) Mg/Mn partitioning as a test for equilibrium between coexisting Fe-Ti oxides. Amer. Mineral. 73(1-2):57–61

Bain AA, Calder ES, Cortés JA, Cortés GP, Loughlin SC (2019) Textural and geochemical constraints on andesitic plug emplacement prior to the 2004–2010 vulcanian explosions at Galeras volcano, Colombia. Bull. Volcanol. 81(1):1–25

Bain AA, Kendrick JE, Lamur A, Lavallée Y, Calder ES, Cortés JA, Cortés GP, Martinez DG, Torres RA (2021) Micro-textural controls on magma rheology and vulcanian explosion cyclicity. Frontiers. Earth Science 703

Barberi F, Ghigliotti M, Macedonio G, Orellana H, Pareschi MT, Rosi M (1992) Volcanic hazard assessment of Guagua Pichincha (Ecuador) based on past behaviour and numerical models. J. Volcanol. Geotherm. Res. 49:53–68

Befus KS, Andrews BJ (2018) Crystal nucleation and growth produced by continuous decompression of Pinatubo magma. Contrib. Mineral. Petrol. 173(11):1–20

Behrens H, Tamic N, Holtz F (2004) Determination of the molar absorption coefficient for the infrared absorption band of CO_2 in rhyolitic glasses. American Mineral. 89:301–306

Benage MC, Wright H, Coombs ML (2021) Eruption of compositionally heterogeneous andesites from a complex storage region during the 2006 eruption of Augustine Volcano. Bull. Volcanol. 83(3):1–23

Blundy J, Cashman K (2001) Ascent-driven crystallisation of dacite magmas at Mount St. Helens, 1980-1986. Contrib. Mineral. Petrol. 140(6):631–650

Blundy J, Cashman K (2005) Rapid decompression-driven crystallization recorded by melt inclusions from Mount St Helens volcano. Geology 33:793–796

Blundy J, Cashman KV, Rust A, Witham F (2010) A case for CO_2-rich arc magmas. Earth Planet. Sci. Lett. 290(3-4):289–301

Browne BL, Gardner JE (2006) The influence of magma ascent path on the texture, mineralogy, and formation of hornblende reaction rims. Earth Planet. Sci. Lett. 246:161–176

Brugger CR, Hammer JE (2010) Crystallization kinetics in continuous decompression experiments: implications for interpreting natural magma ascent processes. J. Petrol. 51(9):1941–1965

Brugger CR, Johnston AD, Cashman KV (2003) Phase relations in silicic systems at one-atmosphere pressure. Contrib. Mineral. Petrol. 146:356–369

Burgisser A, Poussineau S, Arbaret L, Druitt TH, Giachetti T, Bourdier JL (2010) Pre-explosive conduit conditions of the 1997 Vulcanian explosions at Soufrière Hills Volcano, Montserrat: I. Pressure and vesicularity distributions. J. Volcanol. Geotherm. Res. 194(1-3):27–41

Cashman KV (1988) Crystallization of Mount St. Helens 1980-1986 dacite; a quantitative textural approach. Bull. Volcanol. 50(3):194–209

Cashman KV (2004) Volatile controls on magma ascent and eruption, vol 150. American Geophysical Union Geophysical Monograph Series, Washington DC, pp 109–124

Cashman KV (2020) Crystal size distribution analysis of volcanic samples: advances and challenges. Frontiers in Earth Science 8:291

Cashman KV, Blundy J (2000) Degassing and crystallization of ascending andesite and dacite. Phil. Trans. R. Soc. Lond. 358:1487–1513

Cashman KV, Edmonds M (2019) Mafic glass compositions: a record of magma storage conditions, mixing and ascent. Philos Trans A Math Phys Eng Sci 377(2139):20180004

Cashman KV, Hoblitt RP (2004) Magmatic precursors to the 18 May 1980 eruption of Mount St. Helens, USA. Geology 32(2):141–144

Cashman KV, McConnell S (2005) Multiple levels of magma storage during the 1980 summer eruptions of Mount St. Helens, WA. Bull. Volcanol. 68:57–75

Cassidy M, Cole PD, Hicks KE, Varley NR, Peters N, Lerner AH (2015) Rapid and slow: varying magma ascent rates as a mechanism for Vulcanian explosions. Earth Planet Sci Lett 420:73–84. https://doi.org/10.1016/j.epsl.2015.03.025

Cassidy M, Manga M, Cashman K, Bachmann O (2018) Controls on explosive-effusive volcanic eruption styles. Nat. Comm. 9(1):1–16

Chiodini G, Cioni R, Guidi M, Marini L, Raco B, Taddeucci G (1992) Gas geobarometry in boiling hydrothermal systems: a possible tool to evaluate the hazard of hydrothermal explosions. Acta Vulcanol 2:99–107

Cichy SB, Botcharnikov RE, Holtz F, Behrens H (2011) Vesiculation and microlite crystallization induced by decompression: a case study of the 1991–1995 Mt Unzen eruption (Japan). J. Petrol. 52(7-8):1469–1492

Cioni R (2000) Volatile content and degassing processes in the AD 79 magma chamber at Vesuvius (Italy). Contributions to Mineralogy and Petrology 140(1):40–54

Cioni R, Pistolesi M, Bertagnini A, Bonadonna C, Hoskuldsson A, Scateni B (2014) Insights into the dynamics and evolution of the 2010 Eyjafjallajökull summit eruption (Iceland) provided by volcanic ash textures. Earth Planet. Sci. Lett. 394:111–123

Clarke AB, Stephens S, Teasdale R, Sparks RSJ, Diller K (2007) Petrologic constraints on the decompression history of magma prior to Vulcanian explosions at the Soufrière Hills volcano, Montserrat. J. Volcanol. Geotherm. Res. 161:261–274

Colombier M, Bernard B, Samaniego P, Wright H, Caceres F, Cimarelli C, Heap M, Hess K-U, Vasseur J, Ruthensteiner B, Dingwell D (2022) Cyclic dome-forming to Plinian volcanic activity at Guagua Pichincha Volcano, Ecuador. Bull. Volcanol. (this volume). https://link.springer.com/article/10.1007/s00445-022-01612-1

Couch S, Sparks RSJ, Carroll ML (2003) The kinetics of degassing-induced crystallization at Soufrière Hills Volcano, Montserrat. J. Petrol. 44:1477–1502

Donovan JJ (2002) Probewin (Probe for Windows) 6.11.

Edmonds M, Herd RA, Galle B, Oppenheimer CM (2003) Automated, high time-resolution measurements of SO_2 flux at Soufriere Hills Volcano, Montserrat. Bull. Volcanol. 65(8):578–586

Fornari M, Monzier M, Samaniego P, Robin C, Beate B, Bourdon E, Eissen J-P, Féraud G (2004) Ar-Ar dating of active quaternary Pichincha Volcano, Quito, Ecuador. Geophysical Research Abstracts, p 02442

Gabellini P, Cioni R, Geshi N, Pistolesi M, Miwa T, Lacanna G, Ripepe M (2022) Eruptive dynamics and fragmentation mechanisms during cyclic Vulcanian activity at Sakurajima volcano (Japan): Insights from ash texture analysis. J. Volcanol. Geotherm. Res. 107582

Gaetani GA, O'Leary JA, Shimizu N, Bucholz CE, Newville M (2012) Rapid reequilibration of H_2O and oxygen fugacity in olivine-hosted melt inclusions. Geology 40(10):915–918

Garcia-Aristizabal A, Kamagai H, Samaniego P, Mothes P, Yepes H, Monzier M (2007) Seismic, petrologic, and geodetic analyses of the 1999 dome-forming eruption of Guagua Pichincha, Ecuador. J. Volcanol. Geotherm. Res. 161:333–351

Gaunt HE, Burgisser A, Mothes PA, Browning J, Meredith PG, Criollo E, Bernard B (2020) Triggering of the powerful 14 July 2013 Vulcanian explosion at Tungurahua Volcano, Ecuador. J. Volcanol. Geotherm. Res. 392:106762

Geschwind CH, Rutherford MJ (1995) Crystallization of microlites during magma ascent: the fluid mechanics of 1980–1986 eruptions at Mount St Helens. Bull. Volcanol. 57(5):356–370

Ghiorso MS, Evans BW (2008) Thermodynamics of rhombohedral oxide solid solutions and a revision of the Fe-Ti two-oxide geothermometer and oxygen-barometer. Am J Sci. 308(9):957–1039

Global Volcanism Program (1981) Report on Guagua Pichincha (Ecuador) (McClelland, L., ed.). Scientific Event Alert Network Bulletin, 6:9. Smithsonian Institution. https://doi.org/10.5479/si.GVP.SEAN198109-352020

Global Volcanism Program (1999) Report on Guagua Pichincha (Ecuador) (Wunderman, R., ed.). Bulletin of the Global Volcanism Network, 24:9. Smithsonian Institution. https://doi.org/10.5479/si.GVP.BGVN199909-352020.

Global Volcanism Program (2001) Report on Guagua Pichincha (Ecuador) In: Wunderman R (ed) Bulletin of the Global Volcanism Network, vol 26. Smithsonian Institution, p 1. https://doi.org/10.5479/si.GVP.BGVN200101-352020

Gonnermann HM, Manga M (2013) Dynamics of magma ascent in the. Modeling volcanic processes: the physics and mathematics of volcanism 55

Hall M (1977) El volcanismo en el Ecuador. IPGS Secccion Nacional del Ecuador, Quito, Ecuador, p 120

Hammer JE, Rutherford MJ (2002) An experimental study of the kinetics of decompression-induced crystallization in silicic melt. J. Geophys. Res. 107(B1). https://doi.org/10.1029/2001JB000281

Hammer JE, Cashman KV, Hoblitt RP, Newman S (1999) Degassing and microlite crystallization during pre-climactic events of the 1991 eruption of Mt. Pinatubo, Philippines. Bull. Volcanol. 60:355–380

Hammer JE, Cashman KV, Voight B (2000) Magmatic processes revealed by textural and compositional trends in Merapi dome lavas. J. Volcanol. Geotherm. Res. 100(1-4):165–192

Higgins MD (1994) Numerical modeling of crystal shapes in thin sections: estimation of crystal habit and true size. Am Mineral 79:113–119

Higgins MD (2000) Measurement of crystal size distributions. Am. Mineral. 85(9):1105–1116

Legrand D, Calahorrano A, Guillier B, Rivera L, Ruiz M, Villagómez D, Yepes H (2002) Stress tensor analysis of the 1998–1999 tectonic swarm of northern Quito related to the volcanic swarm of Guagua Pichincha volcano, Ecuador. Tectonophysics 344(1-2):15–36

Lepage LD (2003) ILMAT: an excel worksheet for ilmenite--magnetite geothermometry and geobarometry. Comput Geosci 29(5):673–678

Lindoo A, Cashman KV (2021) High crystal number densities from mechanical damage. Front Earth Sci 9:318

Liu EJ, Cashman KV, Rust AC (2015) Optimising shape analysis to quantify volcanic ash morphology. Geo. Res. J. 8:14–30

Lloyd AS, Plank T, Ruprecht P, Hauri EH, Rose W (2013) Volatile loss from melt inclusions in pyroclasts of differing sizes. Contrib. Mineral. Petrol. 165(1):129–153

Mangler MF, Humphreys M, Wadsworth FB, Iveson AA, Higgins MD (2022) Variation of plagioclase shape with size in intermediate magmas: a window into incipient plagioclase crystallisation. Contrib. Mineral. Petrol. 177(6):1–21

Marsh BD (1988) Crystal size distribution (CSD) in rocks and the kinetics and dynamics of crystallization. Contrib. Mineral. Petrol. 99:277–291

Martel C (2012) Eruption dynamics inferred from microlite crystallization experiments: application to Plinian and dome-forming eruptions of Mt. Pelée (Martinique, Lesser Antilles). J. Petrol. 53(4):699–725

Martel C, Schmidt BC (2003) Decompression experiments as an insight into ascent rates of silicic magmas. Contrib. Mineral. Petrol. 144:397–415

Martel C, Poussineau S (2007) Diversity of eruptive styles inferred from the microlites of Mt Pelée andesite (Martinique, Lesser Antilles). J Volcanol Geotherm Res 166(3–4):233–254. https://doi.org/10.1016/j.jvolgeores.2007.08.003

Martel C, Bourdier J-L, Pichavant M, Traineau H (2000) Textures, water content and degassing of silicic andesites from recent plinian and dome-forming eruptions at Mount Pelée volcano (Martinique, Lesser Antilles arc). J. Volcanol. Geotherm. Res. 96:191–206

Mollard E, Martel C, Bourdier JL (2012) Decompression-induced crystallization in hydrated silica-rich melts: empirical models of experimental plagioclase nucleation and growth kinetics. J. Petrol. 53(8):1743–1766

Monzier M, Samaniego P, Robin C, Beate B, Cotten J, Hall ML, Mothes P, Andrade D, Bourdon E, Eissen J-P, Le Pennec JL, Ruiz AG, Toulkeridis T (2002) Evolution of the Pichincha Volcanic Complex (Ecuador). In: Fifth ISAG. Toulous (France), Extended Abstracts, Institut de Recherche pour le Développement, Paris, pp 429–432

Moore LR, Gazel E, Tuohy R, Lloyd AS, Esposito R, Steele-MacInnis M, Hauri EH, Wallace PJ, Plank T, Bodnar RJ (2015) Bubbles matter: an assessment of the contribution of vapor bubbles to melt inclusion volatile budgets. Amer. Mineral. 100:806–823

Morgan DJ, Jerram DA (2006) On estimating crystal shape for crystal size distribution analysis. J. Volcanol. Geotherm. Res. 154(1-2):1–7

Mothes P, Garcia A, Aguilar J, Viracucha D, Caceras V, Jaramillo R, Stix J, Bonvalot S (2000) Inflationary/deflationary cycles related to repetitive dome growth and destruction as seen in tiltmeter and GPS data: Guagua Pichincha volcano, Ecuador. Eos, Transactions, AGU. 81(48)

Mothes P, Yepes H, Viracucha D, Hall M, Villagómez D (2002) successive dome growth and destruction during recent eruptive activity of Guagua Pichincha Volcano, Ecuador. IAVCEI 1902 Centennial Workshop, Martinique

Murch AP, Cole PD (2019) Using microlites to gain insights into ascent conditions of differing styles of volcanism at Soufrière Hills Volcano. J Volcanol Geotherm Res 384:221–231. https://doi.org/10.1016/j.jvolgeores.2019.07.022

Nakada S, Motomura Y (1999) Petrology of the 1991–1995 eruption at Unzen: effusion pulsation and groundmass crystallization. J. Volcanol. Geotherm. Res. 89(1-4):173–196

Newman S, Lowenstern JB (2002) VolatileCalc: a silicate melt–H2O–CO2 solution model written in Visual Basic for excel. Comput Geosci 28(5):597–604

Newman S, Stolper EM, Epstein S (1986) Measurement of water in rhyolitic glasses; calibration of an infrared spectroscopic technique. Amer. Mineral. 71(11-12):1527–1541

Noguchi S, Toramaru A, Nakada S (2008) Relation between microlite textures and discharge rate during the 1991–1995 eruptions at Unzen, Japan. J Volcanol Geotherm Res 175:141–155. https://doi.org/10.1016/j.jvolgeores.2008.03.025

Ogburn SE, Loughlin SC, Calder ES (2015) The association of lava dome growth with major explosive activity (VEI≥ 4): DomeHaz, a global dataset. Bull. Volcanol. 77(5):1–7

Pardo N, Cronin SJ, Wright HMN, Schipper CI, Smith I, Stewart B (2014) Pyroclast textural variation as an indicator of eruption column steadiness in andesitic Plinian eruptions at Mt. Ruapehu. Bull Volcanol 76:822

Preece K, Gertisser R, Barclay J, Charbonnier SJ, Komorowski JC, Herd RA (2016) Transitions between explosive and effusive phases during the cataclysmic 2010 eruption of Merapi volcano, Java, Indonesia. Bull. Volcanol. 78(8):1–6

Riker JM, Cashman KV, Rust AC, Blundy JD (2015) Experimental constraints on plagioclase crystallization during H2O- and H2O–CO2-saturated magma decompression. J. Petrol. 56:1967–1998

Robin C, Samaniego P, Le Pennec JL, Mothes P, van der Plicht J (2008) Late Holocene phases of dome growth and Plinain activity at Guagua Pichincha volcano (Ecuador). J. Volcanol. Geotherm. Res. 176:7–15

Roman DC, Cashman KV, Gardner CA, Wallace PJ, Donovan JJ (2006) Storage and interaction of compositionally heterogeneous magmas from the 1986 eruption of Augustine Volcano, Alaska. Bull. Volcanol. 68:240–254

Rust AC, Cashman KV, Wallace PJ (2004) Magma degassing buffered by vapor flow through brecciated conduit margins. Geology 32(4):349–352

Rutherford MJ, Devine JD (2003) Magmatic conditions and magma ascent as indicated by hornblende phase equilibria and reactions in the 1995-2002 Soufrière Hills Magma. J. Petrol. 44(8):1433–1454

Rutherford MJ, Hill PM (1993) Magma ascent rates from amphibole breakdown; an experimental study applied to the 1980-1986 Mount St. Helens eruptions. J. Geophys. Res. 98(11):19,667–19,685

Schneider CA, Rasband WS, Eliceiri KW (2012) NIH Image to ImageJ: 25 years of image analysis. Nat. Methods 9:671–675

Shea T, Hammer JE (2013) Kinetics of cooling-and decompression-induced crystallization in hydrous mafic-intermediate magmas. J. Volcanol. Geotherm. Res. 260:127–145

Spilliaert N, Allard P, Métrich N, Sobolev AV (2006) Melt inclusion record of the conditions of ascent, degassing, and extrusion of volatile-rich alkali basalt during the powerful 2002 flank eruption of Mount Etna (Italy). J. Geophys. Res. 111(B4)

Stormer JC (1983) The effects of recalculation on estimates of temperature and oxygen fugacity from analyses of multicomponent iron-titanium oxides. Am. Mineral. 68(5-6, 586):–594

Suzuki Y, Gardner JE, Larsen JF (2007) Experimental constraints on syneruptive magma ascent related to the phreatomagmatic phase of the 100AD eruption of Usu volcano, Japan. Bull. Volcanol. 69:423–444

Suzuki Y, Maeno F, Nagai M, Shibutani H, Shimizu S, Nakada S (2018) Conduit processes during the climactic phase of the Shinmoedake 2011 eruption (Japan): insights into intermittent explosive activity and transition in eruption style of andesitic magma. J Volcanol Geotherm Res 358:87–104

Taddeucci J, Pompilio M, Scarlato P (2004) Conduit processes during the July–August 2001 explosive activity of Mt. Etna (Italy): inferences from glass chemistry and crystal size distribution of ash particles. J. Volcanol. Geotherm. Res. 137(1-3):33–54

Toramaru A, Noguchi S, Oyoshihara S, Tsune A (2008) MND (microlite number density) water exsolution rate meter. J. Volcanol. Geotherm. Res. 175(1-2):156–167

Torres R, Kumagai H, Taguchi K (2021) Source models of long-period seismic events at Galeras volcano, Colombia. Geophys J Int 227(3):2137–2155. https://doi.org/10.1093/gji/ggab325

Vetere F, Iezzi G, Behrens H, Cavallo A, Misiti V, Dietrich M, Knipping J, Ventura G, Mollo S (2013) Intrinsic solidification behaviour of basaltic to rhyolitic melts: a cooling rate experimental study. Chem. Geol. 354:233–242

Villagómez D (2000) Sismicidad del volcan Guagua Pichincha, 1998-1999. Departamento de Geologia, Escuela Politecnica Nacional, Quito, Ecuador, thesis, p 114

Wallace PJ (2005) Volatiles in subduction zone magmas: concentrations and fluxes based on melt inclusion and volcanic gas data. J. Volcanol. Geotherm. Res. 140(1-3):217–240

Waters LE, Lange RA (2015) An updated calibration of the plagioclase-liquid hygrometer-thermometer applicable to basalts through rhyolites. Am Mineral 100:2172–2184

White R, McCausland W (2016) Volcano-tectonic earthquakes: a new tool for estimating intrusive volumes and forecasting eruptions. J. Volcanol. Geotherm. Res. 309:139–155

Wolf KJ, Eichelberger JC (1997) Syneruptive mixing, degassing, and crystallization at Redoubt Volcano, eruption of December, 1989 to May 1990. J. Volcanol. Geotherm. Res. 75:19–37

Wright HMN, Cashman KV, Rosi M, Cioni R (2007) Breadcrust bombs as indicators of Vulcanian eruption dynamics at Guagua Pichincha volcano, Ecuador. Bull. Volcanol. 69:281–300

Wright HM, Cashman KV, Mothes PA, Hall ML, Ruiz AG, Le Pennec JL (2012) Estimating rates of decompression from textures of erupted ash particles produced by 1999–2006 eruptions of Tungurahua volcano, Ecuador. Geology 40(7):619–622